Bulletin of the Seismological Society of America

This copy is for distribution only by
the authors of the article and their institutions
in accordance with the Open Access Policy of the
Seismological Society of America.

For more information see the publications section
of the SSA website at www.seismosoc.org

THE SEISMOLOGICAL SOCIETY OF AMERICA
400 Evelyn Ave., Suite 201
Albany, CA 94706-1375
(510) 525-5474; FAX (510) 525-7204
www.seismosoc.org

Bulletin of the Seismological Society of America, Vol. 105, No. 4, pp. –, August 2015, doi: 10.1785/0120140297

Development of a Response Spectral Ground-Motion Prediction Equation (GMPE) for Seismic-Hazard Analysis from Empirical Fourier Spectral and Duration Models

by Sanjay Singh Bora,* Frank Scherbaum,† Nicolas Kuehn, Peter Stafford, and Benjamin Edwards‡

Abstract Empirical ground-motion prediction equations (GMPEs) require adjustment to make them appropriate for site-specific scenarios. However, the process of making such adjustments remains a challenge. This article presents a holistic framework for the development of a response spectral GMPE that is easily adjustable to different seismological conditions and does not suffer from the practical problems associated with adjustments in the response spectral domain. The approach for developing a response spectral GMPE is unique, because it combines the predictions of empirical models for the two model components that characterize the spectral and temporal behavior of the ground motion. Essentially, as described in its initial form by Bora *et al.* (2014), the approach consists of an empirical model for the Fourier amplitude spectrum (FAS) and a model for the ground-motion duration. These two components are combined within the random vibration theory framework to obtain predictions of response spectral ordinates. In addition, FAS corresponding to individual acceleration records are extrapolated beyond the useable frequencies using the stochastic FAS model, obtained by inversion as described in Edwards and Fäh (2013a). To that end, a (oscillator) frequency-dependent duration model, consistent with the empirical FAS model, is also derived. This makes it possible to generate a response spectral model that is easily adjustable to different sets of seismological parameters, such as the stress parameter $\Delta\sigma$, quality factor Q, and kappa κ_0. The dataset used in Bora *et al.* (2014), a subset of the RESORCE-2012 database, is considered for the present analysis. Based upon the range of the predictor variables in the selected dataset, the present response spectral GMPE should be considered applicable over the magnitude range of $4 \leq M_w \leq 7.6$ at distances $\leq$200 km.

Online Material: GMPE scaling with respect to distance, moment magnitude, V_{S30}, stress parameter and kappa, ratios for various parameters, and median response.

Introduction

When undertaking a probabilistic seismic-hazard analysis (PSHA), it is often necessary to make adjustments to published ground-motion prediction equations (GMPEs) to tailor them to the specific site and region in question. Such adjustments have a crucial impact upon the hazard results that are obtained and dictate how realistic the estimates are for the particular setting of the study. In a previous article (Bora *et al.*, 2014), we proposed a physically consistent approach for developing a response spectral GMPE that is easily adjustable to different seismological conditions. The approach presented in Bora *et al.* (2014) was unique in that it involves the derivation of two models as opposed to the classical response spectral GMPEs, which are derived through regression directly on the response spectral ordinates. Essentially, the approach consists of developing an empirical model for the Fourier amplitude spectrum (FAS) and one for the duration of ground motion. Predictions from these two models subsequently are combined

*Also at GFZ German Research Center for Geosciences, Potsdam, Germany.

†On leave from Institute of Earth and Environmental Science, University of Potsdam, Karl-Liebknecht-Street 24-25, 14476 Potsdam, Germany.

‡Now at Department of Earth, Ocean and Ecological Sciences, University of Liverpool, Liverpool L693GP, United Kingdom.

within a random vibration theory (RVT) framework (Cartwright and Longuet-Higgins, 1956) to obtain the predictions of response spectra. Boore (1983, 2003) has demonstrated how it is possible to use RVT to obtain response spectral ordinates using an analytical model for FAS and a measure of duration that is dependent on the earthquake size. The study of Bora *et al.* (2014) introduced a unique measure of ground-motion duration (D_{gm}) that minimized the misfit between the observed response spectra and the RVT-computed response spectra.

As described in Bora *et al.* (2014), the approach of developing an easily adjustable response spectral GMPE can be summarized in four steps: (1) determine the RVT-tuned duration (see the Determination of Duration from Acceleration Records section) for each of the acceleration records in the dataset; (2) derive an empirical duration model (frequency independent); (3) derive an empirical model for the FAS; and (4) obtain the response spectra as a combination of both the empirical models through RVT. In Bora *et al.* (2014), in addition to presenting the approach and the model, we also demonstrated the efficacy of our approach of developing an adjustable response spectral GMPE by considering a simple example of adjusting the high-frequency decay (κ). For instance, although originally introduced by Anderson and Hough (1984) to fit the observed high-frequency fall-off with respect to the Brune's source spectrum (Brune, 1970), κ is often used to represent the site-related attenuation (κ_0) observed in accelerograms. Although, the methodology presented in Bora *et al.* (2014) was at an early stage of development and designed to focus primarily upon issues related to the adjustability of GMPEs, the comparison of response spectral predictions obtained from this approach with those from other classically derived GMPEs (developed from the same database) indicated that our GMPE also can be used as a stand-alone model for predicting response spectra (Douglas *et al.*, 2014).

The present study attempts to address the technical challenges that could not be resolved in Bora *et al.* (2014). In the previous article, we derived a frequency-independent duration model as a function of earthquake magnitude M_w, Joyner–Boore distance R_{JB}, and travel-time-averaged shear-wave velocity over the uppermost 30 m beneath the station (V_{S30}). Therefore, it was not possible to explicitly account for seismological parameters, like the stress parameter $\Delta\sigma$, which controls the high-frequency spectral level in the Brune's source acceleration spectrum and κ_0. In addition, earthquake records possess a useable bandlimited frequency range, in terms of the filter cutoffs in their Fourier spectra, which vary from record to record. Therefore, the number of data points available for regression analysis tends to vary with frequency and the sampling of the predictor variables (of magnitude and distance, etc.) will also vary with frequency as a result. Because of this, the FAS model presented in Bora *et al.* (2014) was derived over a limited frequency range. This limited band of frequencies has a significant impact on how response spectral ordinates at high oscillator frequencies are computed using RVT, particularly for very low values of κ_0. Moreover, in keeping with traditional response spectral GMPEs, the empirical FAS model of Bora *et al.* (2014) also used only M_w, R_{JB}, and V_{S30} as the predictor variables. Importantly, the aleatory variability in the response spectral amplitudes obtained through our initial approach was also significantly larger than those of other GMPEs developed under the same project, with the exception of the model of Bindi *et al.* (2014), as depicted in figure 9 of Douglas *et al.* (2014).

The approach to address these limitations is briefly discussed here and the detailed analysis follows in subsequent sections. To make consistent adjustments to both the FAS and duration models to account for differences in $\Delta\sigma$ and κ_0, we propose an oscillator-frequency-dependent empirical duration model that explicitly includes $\Delta\sigma$ and κ_0 among the predictor variables. In the process of developing empirical models, the records that do not contain a useable Fourier spectral ordinate at a selected frequency usually are discarded. To address this problem, we propose a theoretical model-based extrapolation approach that effectively brings together two different paradigms of ground-motion modeling, that is, the traditional empirical model approach (e.g., Akkar, Sandıkkaya, and Bommer, 2014; Boore *et al.*, 2014) and stochastic ground-motion modeling (e.g., Atkinson and Boore, 2006, 2011; Raghu Kanth and Iyengar, 2007; Douglas *et al.*, 2013; Rietbrock *et al.*, 2013). The approach presented in this study consists of inverting stochastic model parameters from individual spectra using the amplitudes within the useable frequency range. Subsequently, the determined stochastic model parameters are used to predict the FAS beyond the data-supported (useable) frequencies at low and high frequencies. This theoretically extrapolated FAS enables one to use all of the dataset for deriving an empirical FAS model over a wide range of frequencies (ideally at any frequency). Finally, the empirical model for the FAS presented in this study includes $\Delta\sigma$ and κ_0 among the predictor variables in addition to magnitude, distance, and V_{S30}.

The same dataset that was previously used in Bora *et al.* (2014) is also employed herein. The dataset is a subset of the RESORCE-2012 database (Akkar, Sandıkkaya, Şenyurt, *et al.*, 2014), compiled from recordings made across Europe, the Middle East, and the Mediterranean regions and consists of 1232 accelerograms recorded at 355 stations in a source-to-site distance range of $R_{JB} \leq 200$ km, and from earthquakes with magnitudes in the M_w 4.0–7.6 range. All earthquakes considered in this study are shallow crustal events with hypocentral depth $\leq$30 km. In the selected dataset, the station V_{S30} values lie in the 92–2165 m/s range. This study should be considered as an extension of our earlier work and now provides a more holistic framework for developing a physically consistent and easily adjustable GMPE. Consequently, the presented GMPE supersedes our earlier model in Bora *et al.* (2014). Moreover, in the context of recent advancements in site-specific PSHA (Bommer *et al.*, 2014) that involves a single-station sigma concept (Atkinson, 2006; Edwards and Fäh, 2013b; Rodriguez-Marek *et al.*, 2014), we believe that the present approach of developing a response

spectral GMPE will provide a viable option to adjust median predicted ground motions in a physically transparent manner.

In what follows, we first describe the methodological framework of the present approach that includes a comprehensive flow diagram to describe the different steps involved for developing the response spectral GMPE. The Data section contains information about the metadata used in the present analysis, in addition to the criteria used to discard records (more in comparison to the dataset used in Bora *et al.*, 2014) and additional processing done in the present study. This is followed by the description of the FAS model and the determination of its parameters and the subsequent extrapolation of the Fourier spectrum corresponding to the individual records. The derivation of an empirical equation for the FAS is then presented before we determine an oscillator-frequency-dependent duration corresponding to each acceleration trace in the dataset. The determined duration data are used to derive an oscillator-frequency-dependent empirical duration model. Finally, the predicted response spectra are obtained as a combination of the two models. Ⓔ Comparisons of the median predicted response spectra obtained from the presented approach and those from other classical GMPEs are shown in the electronic supplement to this article (Figs. S1–S7). For the detailed description of the RVT method and its implementation in our analysis, the reader is referred to Boore (2003) and Bora *et al.* (2014).

Essence of the Present Approach

The approach of developing a response spectral GMPE in the present article essentially remains the same as used in Bora *et al.* (2014), which combines empirical FAS and duration models of ground motion using the RVT framework. In addition, to extend the useable frequency range of the empirical FAS model, we propose a stochastic model-based extrapolation of the FAS corresponding to individual accelerograms beyond the frequencies supported in the observed data. It is common when processing accelerograms to assign certain limiting values of frequency that define the useable frequency range. These limiting frequencies are generally dictated by either the available sampling rate or by the ambient noise present at low and/or high frequencies. Outside of this range, the observed spectrum is not deemed representative of the actual ground motion, and only the ordinates corresponding to the useable amplitudes are used for deriving the empirical FAS model. The extrapolation scheme being presented here essentially predicts the Fourier spectral amplitudes beyond the frequencies that are supported in the observed data corresponding to individual accelerograms. This scheme requires the determination of stochastic model parameters that are most appropriate for individual spectra. Often these parameters are defined in terms of source, path, and site properties; however, it is also noted that the parameters of the stochastic model determine the level and shape of individual spectra. For example, $\Delta\sigma$ is a measure of the relative strength of the high-frequency amplitudes in a given spectrum (Atkinson and Beresnev, 1997) and may not represent the actual physical property of the source that is often referred to as stress drop. Similarly, κ was originally introduced to fit the high-frequency fall-off of the acceleration spectrum (Anderson and Hough, 1984). Rather than a physical feature, the estimates of $\Delta\sigma$ and κ_0, which are considered to be appropriate for extrapolating the individual spectra in this study, should not be considered as a robust estimate of true source and site properties. The benefit of this extrapolation scheme is that it allows an empirical FAS model to be derived at a wide range of frequencies well beyond the frequency ordinates available in the observed spectra. Moreover, as noted earlier, we derive an oscillator-frequency-dependent empirical model for a unique measure of ground-motion duration (D_{rvto}) corresponding to single-degree-of-freedom (SDOF) system with 5% critical damping. We regard this duration, with the notation D_{rvto}, as unique because it is not estimated directly from the observed acceleration trace, but as an optimizing parameter to match the RVT-based response spectrum (which makes use of the observed FAS) to the observed response spectrum. The method of determining D_{rvto} will be explained in detail in the Oscillator-Frequency-Dependent Duration Model section and can also be found in Bora *et al.* (2014). Finally, predictions from both the empirical models are combined within the RVT framework to obtain the predicted response spectra. A flowchart depicting the entire scheme of the presented approach is shown in Figure 1.

Data

The dataset used in Bora *et al.* (2014) is also used for the present study. It is essentially a subset of the larger parent RESORCE database (Akkar, Sandıkkaya, Şenyurt, *et al.*, 2014). The dataset consists of acceleration traces recorded in Europe, the Mediterranean, and the Middle East. The majority of the records are from Turkey (54.5%), followed by Italy and Greece (31% and 10%, respectively). However, to ensure the validity of the point-source approximation used to extrapolate the Fourier spectra, we discarded a few more records from the dataset that was used in Bora *et al.* (2014). The rejection criterion was based upon magnitude and source-to-site distance in the metadata, accounting for the fact that the large magnitude earthquakes ($M_{\mathrm{w}} > 5.5$) are likely to be associated with extended ruptures that violate the point-source assumption. For events with $M_{\mathrm{w}} < 5.5$, no trace was rejected; for events with $5.5 \leq M_{\mathrm{w}} < 6.5$, traces recorded at hypocentral distance $R < 15$ km were rejected; and, for events with $M_{\mathrm{w}} \geq 6.5$, traces recorded at $R < 30$ km were rejected. This resulted in a reduced dataset with 1200 accelerograms (2400 when including both horizontal components) recorded at 350 stations from 365 earthquakes. In the selected dataset, the station V_{S30} value ranges from 92 to 2165 m/s, out of which 223 station V_{S30} values were measured and the remaining 127 stations have V_{S30} values inferred using different methods. (Ⓔ For details, the reader is referred to the metadata information in Table S1.) The Fourier spectrum of the ground motion was computed from the proc-

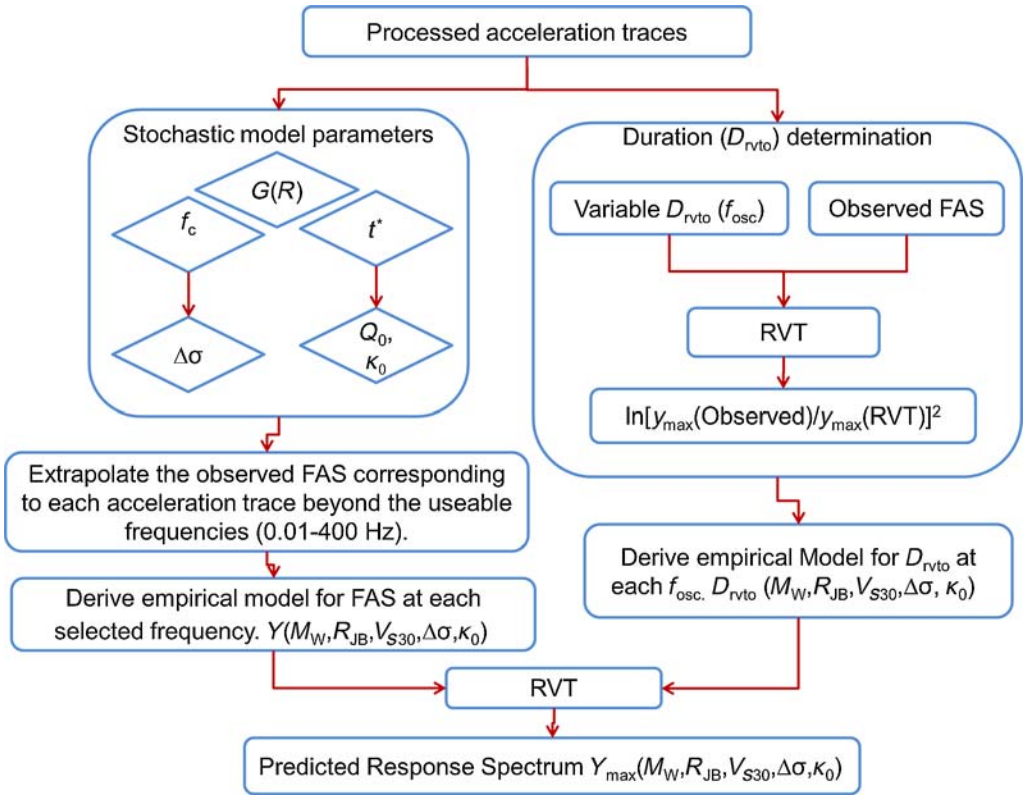

Figure 1. A schematic flowchart of the present approach used for developing a response spectral ground-motion prediction equation. For the detailed information regarding compilation and processing of the RESORCE database, the reader is referred to Akkar, Sandıkkaya, Şenyurt, *et al.* (2014). The color version of this figure is available only in the electronic edition.

essed acceleration traces using the full time series of the given record. However, only the Fourier spectral amplitudes available at useable frequencies were considered in this study. The lower and upper useable frequency limits were decided based upon the cutoff frequencies of the high- and low-pass filters, respectively. An upper limit of 50 Hz was chosen for the records that were not assigned a low-pass frequency. For obtaining smoothed Fourier amplitude at a chosen frequency, we use a Gaussian kernel, which is applied to ordinates at a total of five frequency values (i.e., two on either side of the chosen frequency ordinate).

Determination of Stochastic Ground-Motion Model Parameters

The stochastic ground-motion simulation technique has been used in many parts of the world to model high-frequency ground motions of engineering interest (e.g., Atkinson and Boore, 2006; Edwards and Fäh, 2013b; Rietbrock *et al.*, 2013). This simulation technique employs a simple yet powerful analytical relationship to model the far-field acceleration spectrum of the ground motion using Brune's source model (Brune, 1970, 1971). Subsequently, this source model is modified to accommodate the propagation and site effects on the ground motions obtained at a site as given in the following equation:

$$Y(f) = CM_0G(R)\left[\frac{(2\pi f)^2}{1+\left(\frac{f}{f_c}\right)^2}\right]A(f)\exp(-\pi f t^*), \quad (1)$$

in which $Y(f)$ is the Fourier spectral amplitude at any frequency, f, M_0 is the seismic moment in units of N·m, and f_c is the corner frequency in hertz, given by $f_c = 0.4906\beta(\Delta\sigma/M_0)^{1/3}$ (Eshelby, 1957; Brune, 1970, 1971), in which $\Delta\sigma$ is the stress parameter in megapascals and β (= 3.5 km/s) is the shear-wave velocity near the source. The constant C is generally taken as $C = \Theta_{\lambda\varphi}F\xi/(4\pi\rho\beta^3)$ (Brune, 1970), in which $\Theta_{\lambda\varphi}$ (= 0.55) is the average radiation pattern for S waves (Boore and Boatwright, 1984), F (= 2.0) is the free-surface amplification, ξ (= $1/\sqrt{2}$) is a factor to account for the partition of total shear-wave energy into two horizontal components, and ρ (= 2800 kg/m^3) is the density near the source (Boore, 1983, 2003).

In equation (1), $G(R)$ is the geometrical spreading function, which represents the frequency-independent decay of Fourier amplitudes as a function of distance. In theory, it should equal $1/R$ for an isotropic homogenous whole space, but usually it has been found to be a complex function of distance (Campillo *et al.*, 1984; Atkinson and Mereu, 1992; Edwards *et al.*, 2008; Atkinson and Boore, 2011). At short distances, the geometric spreading is controlled by the decay of direct body-wave amplitudes in a layered crust model, whereas at greater distances there can be contributions from

a combined effect of reflections and refractions from the Moho and a transition to surface-wave spreading.

Therefore, geometrical spreading represents an attenuation regime in a particular geologic and tectonic setting and is often determined from a dataset with a good sampling in terms of distance. The attenuation operator t^* is a combination of the anelastic attenuation represented by the quality factor Q and the parameter kappa κ_0 as given in the following equation (Edwards and Fäh, 2013a):

$$t^* = \frac{R}{Q\beta} + \kappa_0, \tag{2}$$

in which β is the average shear velocity (3.5 km/s) used to infer Q and R is the hypocentral distance. The term κ in equation (2), as defined in the Introduction section, parameterizes the path-independent high-frequency fall-off observed in real accelerograms. Some authors have suggested a frequency-dependent Q model (e.g., Atkinson and Mereu, 1992; Malagnini *et al.*, 2000; Bay *et al.*, 2003; Atkinson, 2004; Drouet *et al.*, 2010) parameterized as

$$Q(f) = Q_0 f^{\alpha}, \tag{3}$$

in which α ranges from 0 (i.e., frequency-independent Q) to 0.9 and Q_0 is the reference value of Q at 1 Hz. However, Edwards *et al.* (2008, 2011) have shown that a frequency-dependent Q model might give a better spectral fit but can lead to a strong trade-off with the frequency-independent geometrical spreading parameter. Moreover, Morozov *et al.* (2008) obtained a spurious frequency-dependent Q model with $\alpha \approx 0.5$ while using a frequency-independent Q for the input numerical simulations. Given that the goal of the present study is to derive an easily adjustable response spectral GMPE, a simple frequency-independent model for Q was considered. In equation (1), $A(f)$ is a function that reflects the effect of the impedance contrast during the wave propagation from the half-space through the upper soil column beneath the site.

As mentioned in the previous section, to extrapolate the spectrum corresponding to individual accelerogram components, we need to determine the stochastic model parameters that are most appropriate for each recording. Usually, the geometrical spreading and Q are determined as an average over the entire dataset; similarly f_c is determined for a common source (Drouet *et al.*, 2008; Edwards and Fäh, 2013a). However, t^* represents a combination of whole-path anelastic attenuation and the near-site attenuation, hence it is determined for each source–site pair (i.e., recordwise; Edwards and Fäh, 2013a). Essentially, the t^* parameter used in this study is equivalent to the original definition of κ of Anderson and Hough (1984) and κ_r of Ktenidou *et al.* (2014). To keep the extrapolation of individual spectra simple and to minimize the discontinuities at the merging frequencies, we determine recordwise values of f_c (and corresponding $\Delta\sigma$) along with the t^*. The recordwise value of f_c may not represent the robust parameter estimate related with the source of an event, yet can be deemed fully consistent within the stochastic model framework as a parameter determining the spectral shape of an individual record. The general scheme for inverting the acceleration spectra for determining the stochastic model parameters involves (1) determination of the geometrical spreading factor from the entire dataset using the vertical components of the given acceleration traces (e.g., Atkinson and Mereau, 1992; Atkinson, 2004; Yenier and Atkinson, 2014), (2) determination of the source corner frequency (f_c) and the attenuation operator (t^*) for each individual accelerogram component (e.g., Thatcher and Hanks, 1973; Scherbaum, 1990), (3) determination of a dataset average Q and a recordwise κ_0 from inverted t^* values, and (4) determination of the site amplification effects at each station from the residuals obtained in a second stage, following this initial inversion. For solving the natural logarithm of equation (1), a nonlinear least-squares fit was performed using Newton's method.

Apparent Geometrical Spreading

The source and attenuation parameters in the stochastic model (equation 1) often exhibit a trade-off with respect to each other (Atkinson and Mereu, 1992; Boore *et al.*, 2010; Yenier and Atkinson, 2014). In an attempt to decouple the effects of geometric spreading and anelastic attenuation, we first determine the geometric spreading function separately and prior to our main inversion scheme. Once the model for the geometric spreading is established, the other stochastic model parameters are determined in subsequent steps. The vertical-component Fourier amplitudes were used to determine the geometrical spreading function, assuming less significant site effects on the records and that they are therefore small enough to be ignored. Moreover, in seismic-hazard related studies the vertical-component spectra are often considered as a proxy for unamplified horizontal-component spectra (Lermo and Chávez-García, 1993; Atkinson and Boore, 2006; Yenier and Atkinson, 2014). In this analysis, and in addition to using the vertical traces, recordings on sites corresponding to $V_{S30} < 180$ m/s are not considered for the determination of geometrical spreading. The vertical-component Fourier spectral amplitudes in the $f = 0.2$–1 Hz range were used to fit the following functional form, assuming a negligible effect of anelastic attenuation in this frequency range:

$$\ln A(f) = s(f) + \ln(CM_0) + \ln G(f, R), \tag{4}$$

in which $A(f)$ is the Fourier spectral amplitude at frequency f and R is the hypocentral distance in kilometers. C and M_0 are the constant and seismic moment, respectively, as defined in equation (1), in which M_0 is computed from the metadata moment magnitudes using the relationship of Hanks and Kanamori (1979). Therefore, $s(f)$ in equation (4) represents the frequency-dependent part of the source spectrum along with the residual site effects. The term $G(f, R)$ refers to the geometrical spreading function corresponding to the selected frequency f. Theoretically, $G(f, R)$ is suggested as a hinged bilinear function of R representing a transition from

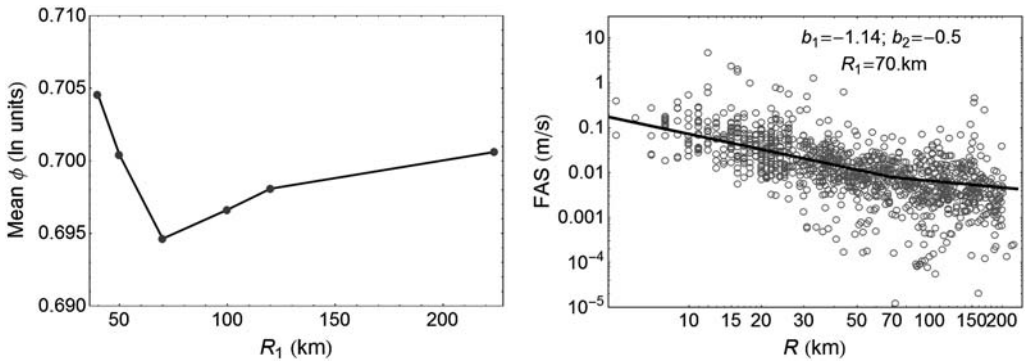

Figure 2. (left) The values of the standard deviation (ϕ) of within-event residuals corresponding to different transition distances R_1 and slope b_1. The minimum ϕ corresponds to $R_1 = 70$ km and $b_1 = -1.14$. (right) The mean Fourier spectral amplitudes (open circles) of vertical components at $f \le 1$ Hz corrected for the source effects using equation (4). The best-fit line with $R_1 = 70$ km and $b_1 = -1.14$ is represented by the thick gray line along with the theoretical value of $b_2 = -0.5$ (Ou and Herrmann, 1990) for hypocentral distance $R > 70$ km.

body-wave to surface-wave distance decay of spectral amplitudes. Some studies (Atkinson and Boore, 1995, 2006, 2011; Edwards *et al.*, 2008) have suggested more complicated functional forms with a trilinear hinged model. However, Mahani and Atkinson (2012) have shown that the linear, bilinear, and trilinear geometrical spreading models do not show significant difference in terms of fitting the data. Hence, in the following discussion, we use a hinged bilinear geometrical spreading model that offers an appropriate balance between simplicity and the ability to model the spectral amplitude decay at both near and far distances:

$$\ln G(f,R) = \begin{cases} b_1(f)\ln R & R \le R_1 \\ b_1(f)\ln R_1 + b_2(f)\ln(R/R_1) & R > R1 \end{cases}, \quad (5)$$

in which R is the hypocentral distance in kilometers. R_1 is the transition distance, and b_1 and b_2 represent the attenuation rates at $R \le R_1$ and $R > R_1$, respectively. A random effects regression as suggested by Abrahamson and Youngs (1992) was performed using equation (4) at eight selected frequency ordinates with smoothed Fourier amplitudes in the $f = 0.2$–1 Hz range. This algorithm separates the residuals into between-event and within-event components that are assumed to be normally distributed with zero mean and standard deviations of τ and ϕ, respectively. To avoid tradeoffs in the determination of slopes, we perform two iterations of the regression. In the first iteration, the regression was performed for different values of transition distance $R_1 = 40$, 50, 70, 100, and 120 km, allowing b_1 and b_2 to take the optimum values corresponding to each R_1. In addition, a straight-line fit was also performed for finding b_1 over the entire distance range. The minimum value of standard deviation for within-event residuals (ϕ) was obtained, corresponding to $R_1 = 70$ km with $b_1 = -1.14$, and the value of $b_2 = -0.46$ is found to be quite close to the theoretically suggested value of -0.5 related with the surface-wave decay in the far-distance range (Ou and Herrmann, 1990). In the second iteration, we fix the value of $b_2 = -0.5$ and perform a regression at each of the R_1 values to find the optimum values of b_1 and R_1. It can be observed in Figure 2, the minimum value of ϕ occurs again, corresponding to $R_1 = 70$ km with $b_1 = -1.14$, although ϕ values corresponding to other combinations of R_1 and b_1 do not differ much. Though the values $R_1 = 70$ km and $b_1 = -1.14$, along with the theoretical value of $b_2 = -0.5$, will be used in the subsequent analysis, the other obtained values of b_1 corresponding to different transition distances were $R_1 = 40$ km and $b_1 = -1.31$, $R_1 = 50$ km and $b_1 = -1.25$, $R_1 = 100$ km and $b_1 = -1.02$, $R_1 = 120$ km and $b_1 = -0.98$, and $R_1 = 224$ km and $b_1 = -0.92$. Although the regression is performed at each of the eight frequency ordinates, average values of b_1 and b_2 are used in terms of the geometrical mean in the selected frequency range to obtain the frequency-independent geometrical spreading function $G(R)$ (as defined in equation 1).

Inversion for f_c and t^*

After constraining the model for the geometric spreading, we invert the observed FAS to determine the attenuation and source parameters. The shape and amplitude of the Fourier spectrum from an observed earthquake at a given distance can be explained in terms of f_c, M_0, and the combined path–site-dependent attenuation operator (t^*). The f_c and t^* are determined for each acceleration record using the entire useable spectrum simultaneously, which was termed as the broadband inversion by Edwards and Fäh (2013a). However, in this study, we determine a record-specific f_c, as opposed to the event-specific value determined by Edwards and Fäh (2013a). As described earlier, the reason for determining the record-specific f_c is to make the extrapolation consistent with the observed spectrum, rather than focusing on a robust parameter determination. Although physically f_c is expected to vary from record to record, depending upon the directional and directivity effects (Madariaga, 1976), one might expect to capture site effects if determining recordwise f_c from empirical spectra. Therefore, after fixing the geometrical spreading factor, f_c and t^* were allowed to vary for an individual spectrum while using the metadata moment

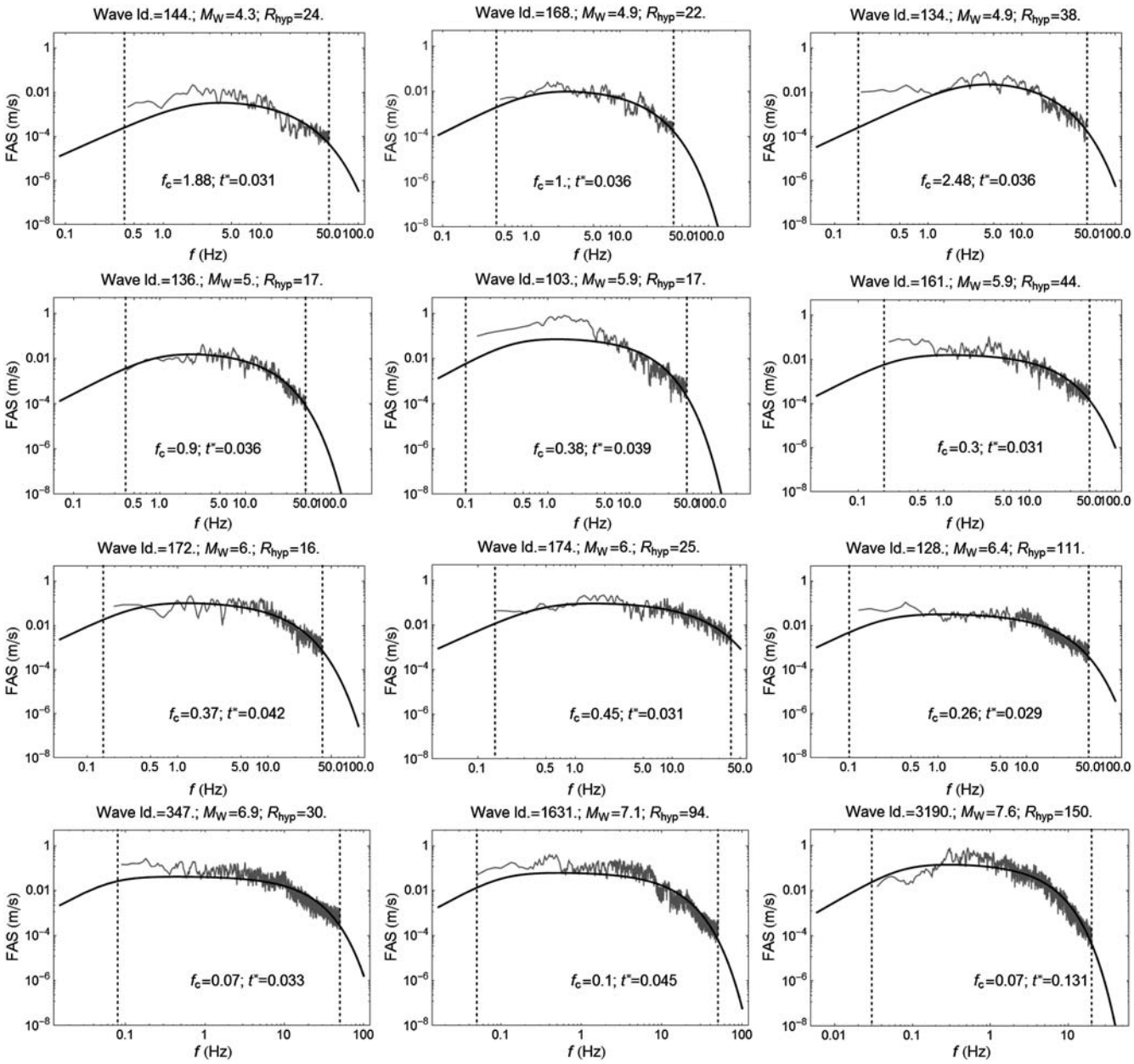

Figure 3. Plots depicting the fit between the rock (V_{S30} = 620 m/s) normalized Fourier amplitude spectrum (FAS; thin gray lines), modeled FAS (thick dark gray lines), and the lower and upper limits of the useable frequency (vertical dashed lines). The Fourier spectral amplitudes between the useable frequency limits are used for inversion.

magnitude (M_w) and the previously determined geometrical spreading model to determine the low-frequency spectral level. The source f_c was limited such that it could vary within the 0.1–100 MPa $\Delta\sigma$ range. Similarly, the t^* values were also allowed to vary in a range corresponding to Q = 200–2000 and κ_0 = 0.001–0.08 s. In addition, observed spectra are adjusted such that they correspond to the same reference shear-wave velocity of 620 m/s. We assume that the generic rock velocity profile of California (Boore and Joyner, 1997) anchored at V_{S30} = 620 m/s is suitable for the dataset used here. The reference crustal amplification was computed using the quarter-wavelength approximation (Joyner *et al.*, 1981; Boore and Joyner, 1997). Figure 3 depicts the plots of observed FAS normalized to the reference rock (V_{S30} = 620 m/s) and the fitted FAS corresponding to some selected records to demonstrate the representative performance of the fitted model.

Attenuation (Q and κ_0)

The combined attenuation operator t^* values obtained from the previous stage were used to decouple the frequency-independent whole-path attenuation Q and the high-frequency attenuation κ_0 commonly attributed to the propagation effects

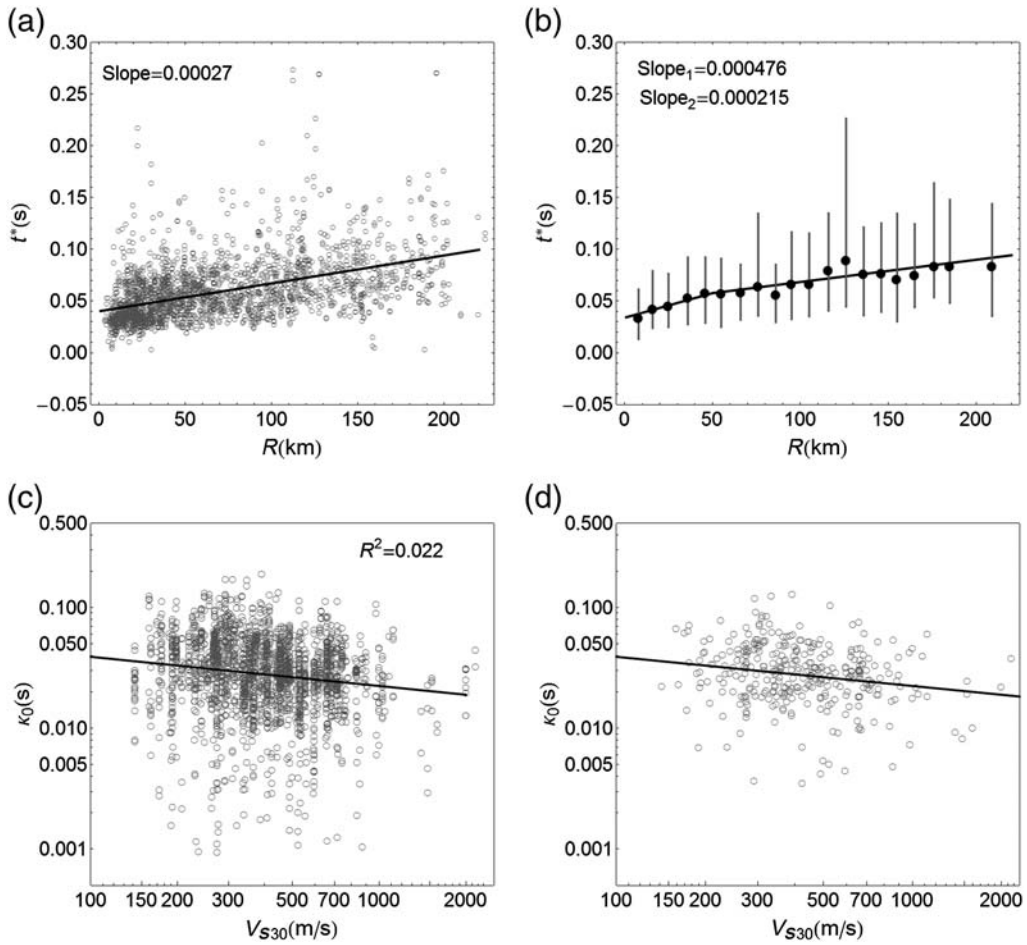

Figure 4. (a) Inverted combined attenuation operator (t^*) values (open circles) compared with hypocentral distance (R), along with the best-fit linear relationship (thick gray line). (b) The mean t^* values relative to distance; the mean t^* is computed in each distance bin of 10 km. The edges of the gray vertical bars indicate the values corresponding to 5% and 95% quantiles of t^* values in each distance bin. The fitted bilinear relationship in equation (6) is depicted by the (thick) dark gray line. (c) The record-specific high-frequency attenuation parameter (κ_0) values (open circles) are plotted against the corresponding V_{S30} values, and the thick gray line represents the best-fit relationship in equation (7). (d) The same plot as in (c) but for station-specific κ_0 values for which the median value of all the record κ_0 values at a station is chosen to represent the station-specific κ_0.

in the uppermost layer of soil and rock beneath the recording site. In Figure 4a, a straightforward way for determining contributions from Q and κ_0 from the dataset is to perform a linear regression of the inverted t^* values against distance and then relate the slope of the fitted line to Q using the relationship given in equation (2), in which the intercept represents an average value of κ_0 associated with the selected dataset. The slope of the fitted line with the 95% confidence interval was determined as 0.000269 ± 0.00002, which gives $Q = 1059$ with the limits 985 and 1145, assuming a shear-wave velocity $\beta = 3.5$ km/s. The intercept representing the average site term κ_0 was found to be $\kappa_0 = 0.0401 \pm 0.00171$ s. In Figure 4b, the plot of mean t^* values in each 10 km distance bin is depicted, which indicates a steeper slope within 50 km followed by a relatively lower increase in t^* values with distance. This bilinear form of the relationship between t^* and distance indicates a 1D Q model (Edwards *et al.*, 2008, 2011) with a higher attenuating zone at shallower depths followed by a less attenuating elastic half-space. We do not investigate a depth-dependent (frequency-independent) Q structure in this study because it requires an assumption of the velocity structure that is not available with the present dataset. Nevertheless, to capture this distance-dependent slope of the $t^* - R$ relationship, we fit the data with a bilinear form as

$$t^* = k_0 + \begin{cases} \text{Slope}_1 R & R \le 50 \text{ km} \\ \text{Slope}_1 50 + \text{Slope}_2 (R - 50) & R > 50 \text{ km} \end{cases}. \quad (6)$$

The two slopes determined by fitting the data with the bilinear relationship used in equation (6) give values of Q as 600 and 1327 at distances $R \le 50$ and $R > 50$ km, respectively, assuming a shear-wave velocity of 3.5 km/s. The record-specific value of κ_0 is obtained by correcting the corresponding t^* value (at a distance R) for this bilinear slope that essentially extrapolates it to $R = 0$ km. The average of these record-specific κ_0 values at a station gives the station-specific κ_0 (Van Houtte *et al.*, 2011). Often, κ_0 is observed to

indicate a weak correlation with the measured V_{S30} values (Edwards *et al.*, 2011; Van Houtte *et al.*, 2011; Edwards and Fäh, 2013a). Figure 4c and 4d depict this $V_{S30} - \kappa_0$ correlation for record-specific and station-averaged κ_0 values, respectively. The site-specific average κ_0 values are computed as the median, assuming a lognormal distribution. The determined regression line for a log–log (natural-log) relationship with extremely weak coefficient of determination $R^2 = 0.022$ is obtained as

$$\ln(\kappa_0) = -2.126 - 0.241 \ln(V_{S30}). \quad (7)$$

The correlation of κ_0 with V_{S30} determined from this dataset is relatively weak in comparison to some other studies (Van Houtte *et al.*, 2011; Edwards and Fäh, 2013a). Limited sampling in terms of sites with high V_{S30} values represented in the dataset could be one of the reasons for this lower correlation.

Site Amplification

The site amplification curves corresponding to each station were determined using the residuals obtained during the first stage inversion (Edwards *et al.*, 2008; Drouet *et al.*, 2010; Edwards and Fäh, 2013a). The amplification at each frequency was computed as the geometric mean of all the factorial residuals, that is, observed $Y(f)$/modeled $Y(f)$ at that frequency overall spectra recorded at a given site. This approach has been shown to provide amplification consistent with expected 1D behavior at rock sites and more complex 2D or 3D behavior at soil (Edwards *et al.*, 2013; Michel *et al.*, 2014). The catalog-based moment magnitude was used at the first stage of inversion for determining the low-frequency spectral level. To use as much data as possible for developing the GMPE, the site amplification curves were computed for all the stations. The selected dataset includes a total of 350 stations; however, there are only 141 stations that have ≥ 3 records. Therefore, for stations recording fewer records, the estimated site amplification curves cannot be considered as a robust estimate of true site amplification effects because it will certainly be capturing aleatory variability as well.

The generic rock site ($V_{S30} = 620$ m/s) for which the Fourier spectra have been corrected can be assumed as the reference for the site amplification curves presented in this study; that is, all amplifications are relative to a site with 620 m/s. Figure 5 depicts the site amplification curves for a selection of stations. We believe that the site amplification curves presented here represent multiple effects together, for example, the actual amplification due to the upper soil layers beneath the station, the residual path effects which could not be modeled and certain other unmodeled phenomena, as well as inherent variability and noise.

Source Parameters f_c and $\Delta\sigma$

Inverted f_c values are plotted against the metadata moment magnitude M_w in Figure 6. It may be noted that the f_c values were determined for each record in this study; however, in Figure 6 the average in terms of median value (assuming a lognormal distribution) corresponding to an event is used. The regression line determined from this dataset gives the following relationship:

$$\log_{10}(f_c) = 2.46(\pm 0.13) - 0.49(\pm 0.025) \times M_w, \quad (8)$$

which is found to be effectively equivalent to a constant $\Delta\sigma$ model. If a constant $\Delta\sigma$ model is assumed to be appropriate, then the relationship between f_c and M_w becomes

$$\log_{10}(f_c) = 2.52(\pm 0.016) - 0.5 \times M_w. \quad (9)$$

The median value of the $\Delta\sigma$, assuming the constant $\Delta\sigma$ model, was found to be 8.4 MPa, with a lognormal standard deviation of 1.1. The $\Delta\sigma$ corresponding to the inverted f_c (Hz) value can be obtained using the relationship,

$$\Delta\sigma = M_0 \left(\frac{f_c}{0.4906\beta} \right)^3 \quad (10)$$

(Eshelby, 1957; Brune, 1970, 1971), in which β is the near-source velocity (assumed to be 3.5 km/s) and the M_0 (in N·m) is determined from the moment magnitude in the database using the relationship from Hanks and Kanamori (1979). In addition, the magnitude dependence of $\Delta\sigma$ was also investigated by selecting the f_c values corresponding to $M_w \leq 5$ separately. The $f_c - M_w$ relationship for events with $M_w \leq 5$ is also quite close to the constant $\Delta\sigma$ model. However, it should also be noted that events with $M_w > 6$ are not well represented in the selected dataset, making it difficult to resolve a magnitude dependence of $\Delta\sigma$.

Extrapolation of the Observed FAS

After determining the stochastic model parameters, the FAS corresponding to each record was extrapolated beyond the filter cutoffs toward the low- and high-frequency ends of the spectrum. To perform extrapolation, the record-specific f_c and t^* values, along with the derived geometric spreading function, were used. The site effects in terms of station-specific site amplification curves were used for making the forward prediction. To extrapolate the spectrum beyond the upper useable frequency, the spectrum is up-sampled with a common Nyquist frequency of 400 Hz and padded with zeroes beyond the upper useable frequency (Boore and Goulet, 2014). Subsequently, the padded zeroes were replaced by the stochastic model predicted amplitudes in this frequency range. Similarly, for extrapolating toward the low frequencies, we select a new minimum frequency (f_2) to be 0.01 Hz and pad n zeroes between the f_2 and actual minimum frequency in which n is given by

$$n = \frac{1}{dt_{\text{samp}} \times f_2} - n_0. \quad (11)$$

In equation (11), dt_{samp} is the original sampling rate and n_0 is the number of data points in the observed record. Subsequently, those low-frequency padded zeroes were replaced by the stochastic-model-generated amplitudes. For each

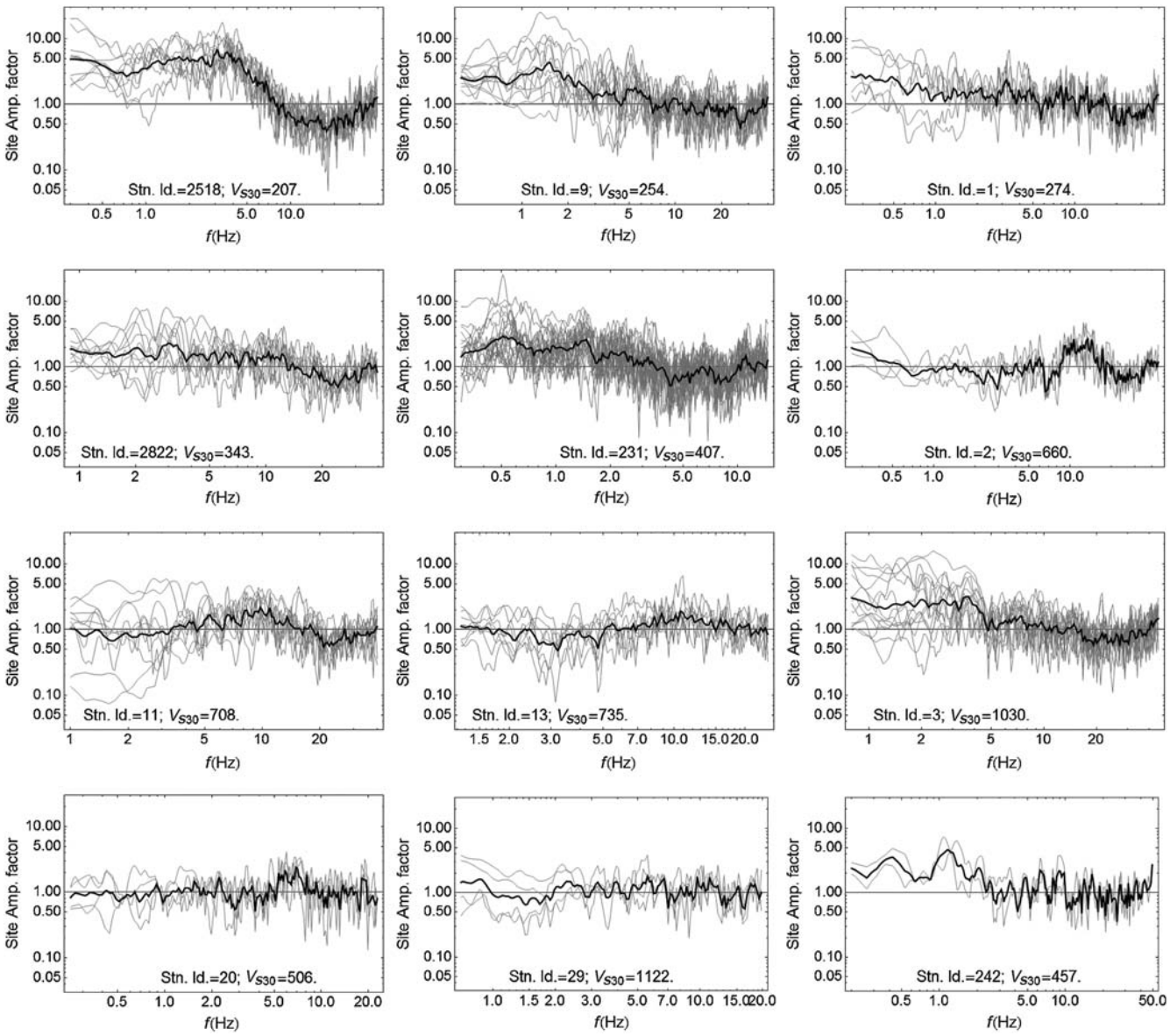

Figure 5. Representative site amplification plots. The thin gray curves indicate the residuals corresponding to the each record. The thick gray curve represents the geometric mean of all the record residuals (in linear space) considered as the site amplification curve to the corresponding station.

record, beyond the useable frequency limits, the stochastic-model-generated Fourier amplitudes were used to extrapolate the corresponding spectrum; whereas the observed amplitudes between the useable frequency limits were retained. Consequently, we get FAS corresponding to individual records ranging from 0.01 to 400 Hz. This enables one to use all the frequencies in this range for deriving an empirical model for the FAS. The FAS for a subset of the records depicted in Figure 3 are extrapolated beyond the useable frequency limits along with the observed FAS; these are depicted in Figure 7.

Regression Model for the FAS

For deriving the empirical model for the FAS, we chose a similar functional form as used in Bora *et al.* (2014) but added functional terms for two additional predictor variables $\Delta\sigma$ and κ_0. Assuming a lognormal distribution of Fourier spectral amplitudes at each frequency, the median model used for regression is

$$\ln Y(f) = c_0 + c_1 M_w + c_2 M_w^2 + c_3 \ln(\Delta\sigma) + (c_4 + c_5 M_w) \ln\left(\sqrt{R_{JB}^2 + c_6^2}\right) - c_7 \sqrt{R_{JB}^2 + c_6^2} + c_8 \ln(V_{S30}) - c_9 \kappa_0. \quad (12)$$

In the above equation, Y is the Fourier spectral amplitude in meters per second of each individual accelerogram component at frequency f, M_w is the moment magnitude, R_{JB} is the closest distance from the recording site to the surface projection of

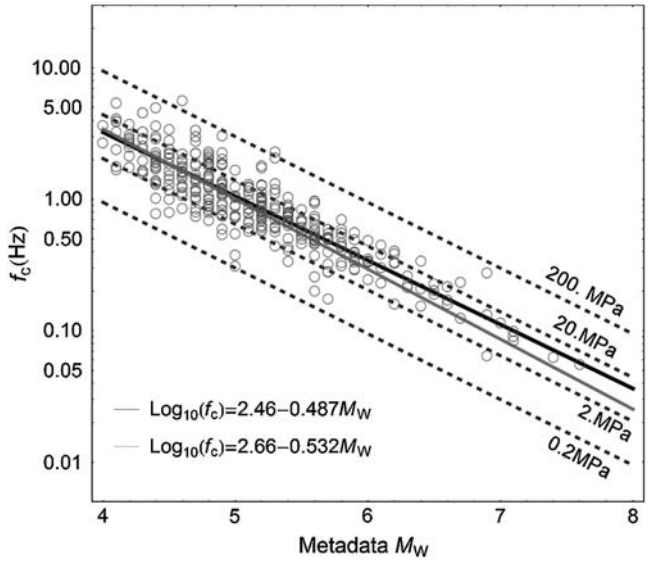

Figure 6. The event-specific f_c (source corner frequency) values (open circles) against moment magnitude M_w for which the median of all the record f_c values (for an event) is chosen to represent the event-specific f_c values. The thick dark-gray line is the best-fit line to the observed relationship for the entire dataset. Thick light-gray line depicts the same relationship only for $M_w \leq 5$ earthquakes. The dashed gray lines depict the lines of constant $\Delta\sigma$ (stress parameter).

the rupture, and V_{S30} is the time-averaged shear-wave velocity in the upper 30 m of the soil column beneath the recording site. For performing regression, the record-specific values of the predictor variables $\Delta\sigma$ and κ_0 are used. As described earlier, the record-specific f_c values are used to obtain the record-specific $\Delta\sigma$ values. The record-specific κ_0 values are obtained by correcting corresponding t^* for the slope of the bilinear t^*–distance relationship using equation (6). The regression coefficients involved in equation (12) were determined using the random effects algorithm of Abrahamson and Youngs (1992). The total standard deviation (σ) associated with the median logarithmic Fourier spectral amplitude at each frequency f was computed using τ and ϕ:

$$\sigma = \sqrt{\tau^2 + \phi^2}. \tag{13}$$

The regression was performed on the smoothed Fourier spectral amplitudes at selected frequency ordinates between 0.01 and 400 Hz. The spacing of 0.08 in natural-log units resulted in 58 frequency ordinates from 0.01 to 363.08 Hz. The regression was performed at each of the 58 frequencies; values of the coefficients involved in equation (12) are listed in Table 1, along with values of τ, ϕ, and σ. It is worth mentioning here that we do not smooth the coefficients for predicting the FAS. For checking the robustness of the derived model, the regression residuals are plotted against the predictor variables magnitude, distance, V_{S30}, $\Delta\sigma$, and κ_0 involved in equation (12) at $f = 0.48$, 5.25, and 15.85 Hz and are shown here in Figure 8. In Figure 8, the dispersion of the residuals is observed to decrease toward higher frequencies (at 5.25 and 15.85 Hz). The greater dispersion of the within-event residuals at low frequencies can be attributed mainly to the site amplification effects that the simple proxy (V_{S30}) may not be able to model beyond a certain extent. However, a large reduction observed in the residuals of the predicted FAS can be attributed to the inclusion of record-specific values of $\Delta\sigma$ and κ_0 parameters. Therefore, the reduction obtained here may not represent the true decrease in ground-motion variability if the event-specific $\Delta\sigma$ and station-specific κ_0 values would have been used. Nevertheless, the median of the GMPE should be considered consistent and valid within the range of the predictor variable values irrespective of the predictor variable definition, that is, whether it is event/station specific or record specific. The scaling of median Fourier amplitude spectra with all the predictor variables involved in equation (12) is depicted in Figure 9. Figure 9a shows magnitude scaling of the entire spectrum at $R_{JB} = 30$ and 100 km, respectively. A magnitude–corner-frequency relationship can be readily observed. Figure 9b depicts the scaling of Fourier spectral ordinates with respect to magnitude at $f = 0.5$, 5, and 15 Hz. Similarly, Figure 9c represents the scaling of Fourier spectral ordinates with respect to distance at these same frequencies for magnitudes of $M_w = 5$ and 7, whereas Figure 9d depicts the scaling with respect to $\Delta\sigma$ for the same magnitudes. The influence of the $\Delta\sigma$ beyond the corner frequency is visible. Fourier spectral ordinates beyond a certain frequency (3 Hz), for the similar attenuation conditions, are solely determined by the $\Delta\sigma$ irrespective of earthquake magnitude. A similar plot is depicted in Figure 9f, representing scaling of Fourier spectrum with κ_0 for two different values of $\Delta\sigma$. Often the $\Delta\sigma$ is observed to control the high-frequency amplitudes; however, κ_0 is also expected to reduce the high-frequency amplitudes depending upon its magnitude. The scaling of the Fourier spectrum with V_{S30} is depicted in Figure 9e at two different source-to-site distances, $R_{JB} = 30$ and 150 km. The $V_{S30} - \kappa_0$ relationship in equation (7) is used to obtain the κ_0 values corresponding to the different V_{S30} values used in all parts of Figure 9. The stiffness of the profile is observed to have a larger impact on the low-frequency spectral amplitudes than at the high-frequency amplitudes. Such behavior can be attributed to the site term used in equation (12) that does not include nonlinear site behavior.

Oscillator-Frequency-Dependent Duration Model

The stochastic simulation method of Boore (1983, 2003) assumes that the radiated energy from an earthquake source can be characterized by a process exhibiting spectral stationarity with energy released over a duration equal to the rise time (the inverse of the corner frequency f_c). Moreover, the computation of response spectral ordinates using the RVT method also requires an estimate of ground-motion duration (Vanmarcke and Lai, 1980; Hanks and McGuire, 1981; Boore, 1983; Boore and Thompson, 2014). There are multiple definitions of duration in the literature and the choice of a particular type is driven by its suitability for a particular application (Bommer and Martínez-Pereira, 1999). Bora *et al.*

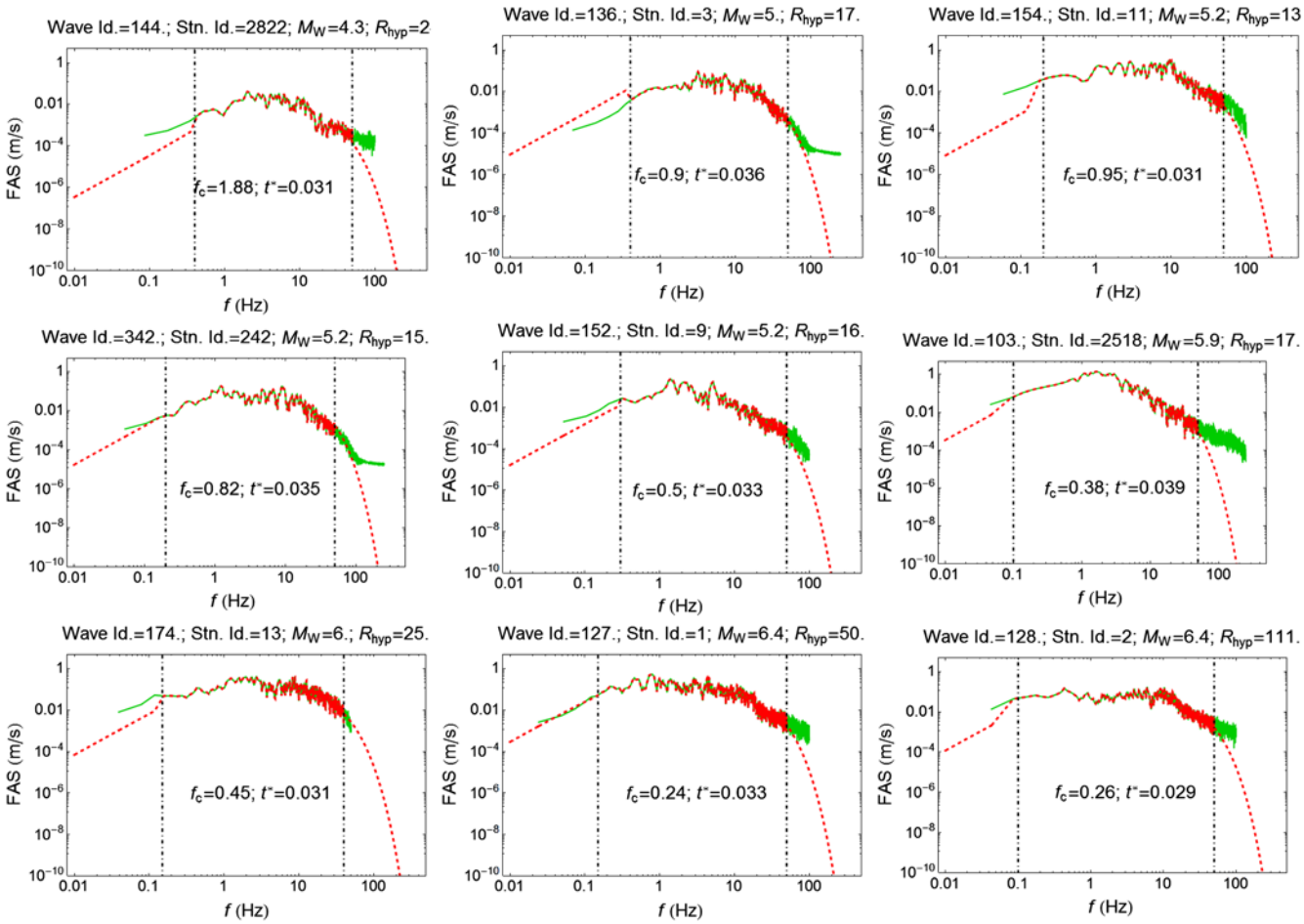

Figure 7. Extrapolation of the observed FAS. The thin solid curves indicate the observed FAS, and bold dashed curves correspond to the extrapolated FAS. Vertical dashed-dotted lines depict the lower and upper limits of the useable frequency respectively. The effect (discontinuity) of stationwise site amplification (shown in Fig. 5) on extrapolation can be seen at the merging frequencies. The plots are shown for a subset of the plots shown in Figure 3. The color version of this figure is available only in the electronic edition.

(2014) proposed another measure of duration D_{gm} that is different from most others in that it is not determined directly from the recorded acceleration trace. However, it is tied very closely to the RVT framework. The computation of response spectral ordinates using the RVT method depends upon the FAS (model) and duration of ground motion (Boore, 2003; Boore and Thompson, 2012; Bora *et al.*, 2014). We define the duration as having the value that is required for a response spectral ordinate computed using RVT, given the FAS of the record, to be equal to that of the observed record. Similar measures of duration were also determined by Vanmarcke and Lai (1980) and Atkinson (1993) for peak ground acceleration (PGA) and peak ground velocity, respectively, though Bora *et al.* (2014) and this study use response spectral ordinates of acceleration motion. The approach for estimating this duration can be summarized in two steps: (1) compute the FAS from given acceleration trace and (2) use this FAS as the input to RVT and solve for the duration (the only remaining unknown) in such a way that the mismatch between the RVT-computed response spectrum and the observed response spectrum is minimized. This process involves minimization of the mismatch between the two response spectral amplitudes (RVT based and observed) at different oscillator frequencies corresponding to an SDOF system with 5% damping. This method of duration estimation from an acceleration trace is unique in that it was derived with the purpose of being used within the RVT framework. Therefore, we suggest a different name for the duration determined using this approach: "RVT-optimized duration," with the notation D_{rvto}. The choice of an oscillator-frequency-dependent D_{rvto} over a constant D_{gm} is to enable the most reliable estimates of the response spectral ordinates. In addition, an oscillator-frequency-dependent D_{rvto} model will allow for consistent adjustments in duration estimates corresponding to different values of seismological parameters, such as $\Delta\sigma$ and κ_0 at a selected oscillator frequency.

Determination of Duration (D_{rvto}) from Acceleration Records

As noted previously, the computation of response spectral ordinates through the RVT method uses the FAS and

Table 1
Coefficients Associated with the Median Prediction of Fourier Amplitude Spectrum (FAS) in Equation (12)

f (Hz)*	c_0	c_1	c_2	c_3	c_4	c_5	c_6	c_7	c_8	c_9	ϕ*	τ*	σ*
0.01	−20.379	3.5	−0.116	−0.04	−2.288	0.304	5.391	0	−0.746	0	0.684	0.568	0.889
0.012	−20.9	3.882	−0.144	−0.027	−2.114	0.276	4.778	0	−0.77	0	0.678	0.598	0.904
0.014	−20.135	3.717	−0.133	−0.029	−2.137	0.282	5.539	0	−0.748	0	0.693	0.601	0.917
0.017	−19.804	3.748	−0.128	−0.025	−2.008	0.258	5.784	0	−0.786	0	0.681	0.609	0.914
0.021	−19.885	3.774	−0.128	−0.022	−1.828	0.227	5.48	0	−0.716	0	0.68	0.636	0.931
0.025	−19.884	4.124	−0.163	−0.028	−1.947	0.235	6.47	0	−0.748	0	0.651	0.63	0.906
0.03	−22.211	4.774	−0.203	−0.02	−1.646	0.176	5.471	0	−0.678	0	0.636	0.639	0.902
0.036	−21.79	4.723	−0.2	−0.013	−1.778	0.194	6.49	0	−0.631	0	0.627	0.647	0.901
0.044	−22.731	5.24	−0.244	−0.014	−1.809	0.192	6.918	0	−0.632	0	0.622	0.659	0.906
0.052	−23.13	5.48	−0.266	−0.014	−1.763	0.186	5.688	0	−0.631	0	0.628	0.674	0.921
0.063	−22.562	5.58	−0.286	−0.024	−1.933	0.205	7.005	0	−0.613	0	0.623	0.651	0.901
0.076	−23.593	5.965	−0.318	−0.012	−1.781	0.182	6.858	0	−0.589	0	0.631	0.711	0.951
0.091	−21.695	5.633	−0.302	−0.016	−1.904	0.199	8.067	0	−0.611	0	0.638	0.707	0.952
0.11	−21.105	5.559	−0.301	0	−1.849	0.195	6.803	0	−0.616	0	0.643	0.729	0.972
0.13	−20.451	5.573	−0.312	0.001	−1.88	0.203	7.353	0	−0.638	0	0.647	0.734	0.978
0.16	−19.753	5.464	−0.309	0.023	−1.854	0.202	7.054	0	−0.64	0	0.656	0.723	0.976
0.19	−19.837	5.708	−0.339	0.046	−1.775	0.195	6.185	0	−0.679	0	0.662	0.735	0.989
0.23	−18.944	5.614	−0.342	0.059	−1.725	0.192	5.744	0	−0.71	0	0.694	0.727	1.005
0.28	−17.322	5.28	−0.327	0.086	−1.763	0.209	4.406	0	−0.752	0	0.726	0.762	1.052
0.33	−16.222	5.04	−0.314	0.1	−1.696	0.202	3.979	0	−0.769	0	0.75	0.748	1.059
0.40	−15.835	5.1	−0.325	0.119	−1.666	0.188	3.828	0	−0.775	0	0.74	0.688	1.010
0.48	−15.055	5.065	−0.325	0.137	−1.596	0.169	3.693	0	−0.826	0	0.753	0.642	0.990
0.58	−13.577	4.716	−0.307	0.148	−1.616	0.175	3.364	0	−0.829	0	0.737	0.606	0.954
0.69	−11.765	4.292	−0.268	0.17	−1.455	0.147	2.944	0	−0.927	0	0.741	0.569	0.934
0.83	−11.191	4.23	−0.264	0.174	−1.435	0.129	3.818	0	−0.916	0	0.717	0.548	0.902
1.00	−10.503	4.015	−0.246	0.196	−1.368	0.112	3.665	0	−0.899	0.011	0.694	0.519	0.867
1.20	−9.776	3.912	−0.246	0.224	−1.401	0.109	4.209	0	−0.886	1.415	0.684	0.51	0.853
1.45	−8.253	3.31	−0.203	0.269	−1.536	0.13	4.619	0	−0.801	1.02	0.668	0.497	0.833
1.74	−10.089	3.619	−0.22	0.307	−1.367	0.086	4.773	0	−0.648	2.758	0.682	0.474	0.831
2.09	−9.409	3.398	−0.215	0.335	−1.472	0.106	5.393	0	−0.579	3.88	0.659	0.431	0.787
2.51	−10.306	3.301	−0.203	0.395	−1.33	0.079	4.686	0	−0.416	5.35	0.646	0.409	0.765
3.02	−7.497	2.439	−0.135	0.436	−1.468	0.09	5.465	0	−0.403	7.578	0.634	0.378	0.738
3.63	−5.929	1.797	−0.093	0.461	−1.7	0.119	6.831	0	−0.253	9.192	0.61	0.356	0.706
4.37	−5.005	1.486	−0.069	0.492	−1.731	0.104	8.502	0	−0.183	11.492	0.624	0.311	0.697
5.25	−4.951	1.694	−0.107	0.524	−2.016	0.139	9.759	0	−0.141	15.453	0.597	0.29	0.664
6.31	−3.559	1.313	−0.09	0.549	−2.358	0.178	10.731	0.001	−0.047	18.729	0.608	0.306	0.681
7.59	−3.94	1.09	−0.074	0.562	−2.421	0.181	10.409	0	0.121	20.416	0.605	0.337	0.693
9.12	−4.262	1.002	−0.075	0.589	−2.305	0.177	9.664	0.002	0.181	25.43	0.592	0.329	0.677
10.97	−4.214	1.114	−0.095	0.612	−2.477	0.213	8.735	0.003	0.115	30.007	0.589	0.3	0.661
13.18	−2.921	0.949	−0.09	0.592	−2.658	0.23	9.346	0.002	0.056	36.76	0.597	0.329	0.682
15.85	−2.308	0.912	−0.088	0.648	−2.672	0.221	9.524	0.002	−0.014	47.137	0.603	0.293	0.670
19.06	−4.21	1.239	−0.116	0.633	−2.456	0.213	6.629	0.006	0.029	55.744	0.58	0.331	0.668
22.91	−3.922	1.301	−0.127	0.641	−2.663	0.238	6.502	0.008	0.007	67.917	0.574	0.332	0.663
27.54	−1.454	1.256	−0.153	0.673	−3.487	0.308	10.695	0.006	−0.009	85.123	0.578	0.312	0.657
33.11	−1.744	1.539	−0.164	0.653	−3.534	0.279	10.273	0.008	−0.055	103.213	0.54	0.348	0.642
39.81	−1.376	2.041	−0.227	0.632	−4.036	0.32	10.923	0.011	−0.103	124.542	0.522	0.59	0.788
47.86	3.241	1.004	−0.164	0.543	−4.839	0.423	11.6	0.013	−0.139	149.351	0.613	0.437	0.753
57.54	1.443	1.458	−0.202	0.64	−4.917	0.393	11.856	0.017	−0.02	180.363	0.497	0.471	0.685
69.18	2.349	1.568	−0.235	0.635	−5.47	0.441	11.877	0.022	−0.016	216.728	0.524	0.525	0.742
83.18	3.359	1.699	−0.273	0.629	−6.116	0.498	11.842	0.028	−0.009	260.454	0.559	0.592	0.814
100.00	4.59	1.917	−0.326	0.622	−6.94	0.567	11.95	0.036	−0.002	313.046	0.605	0.674	0.906
120.23	6.417	2.02	−0.374	0.613	−7.913	0.65	12.003	0.045	0.007	376.273	0.665	0.773	1.020
144.54	8.164	2.247	−0.44	0.603	−9.028	0.747	11.948	0.056	0.017	452.268	0.74	0.893	1.160
173.78	10.179	2.648	−0.534	0.59	−10.435	0.866	12.028	0.068	0.029	543.672	0.836	1.039	1.334
208.93	13.508	2.76	−0.61	0.575	−12.117	1.009	12.076	0.084	0.044	653.547	0.956	1.215	1.546
251.19	16.844	3.11	−0.722	0.556	−14.099	1.178	12.087	0.103	0.062	785.645	1.104	1.427	1.804
302.00	20.879	3.527	−0.855	0.534	−16.485	1.38	12.102	0.125	0.084	944.452	1.287	1.682	2.118
363.08	25.704	4.037	−1.016	0.507	−19.35	1.623	12.117	0.153	0.11	1135.385	1.51	1.991	2.499

*f, frequency; ϕ, within-event standard deviation; τ, between-event standard deviation; σ, total standard deviation.

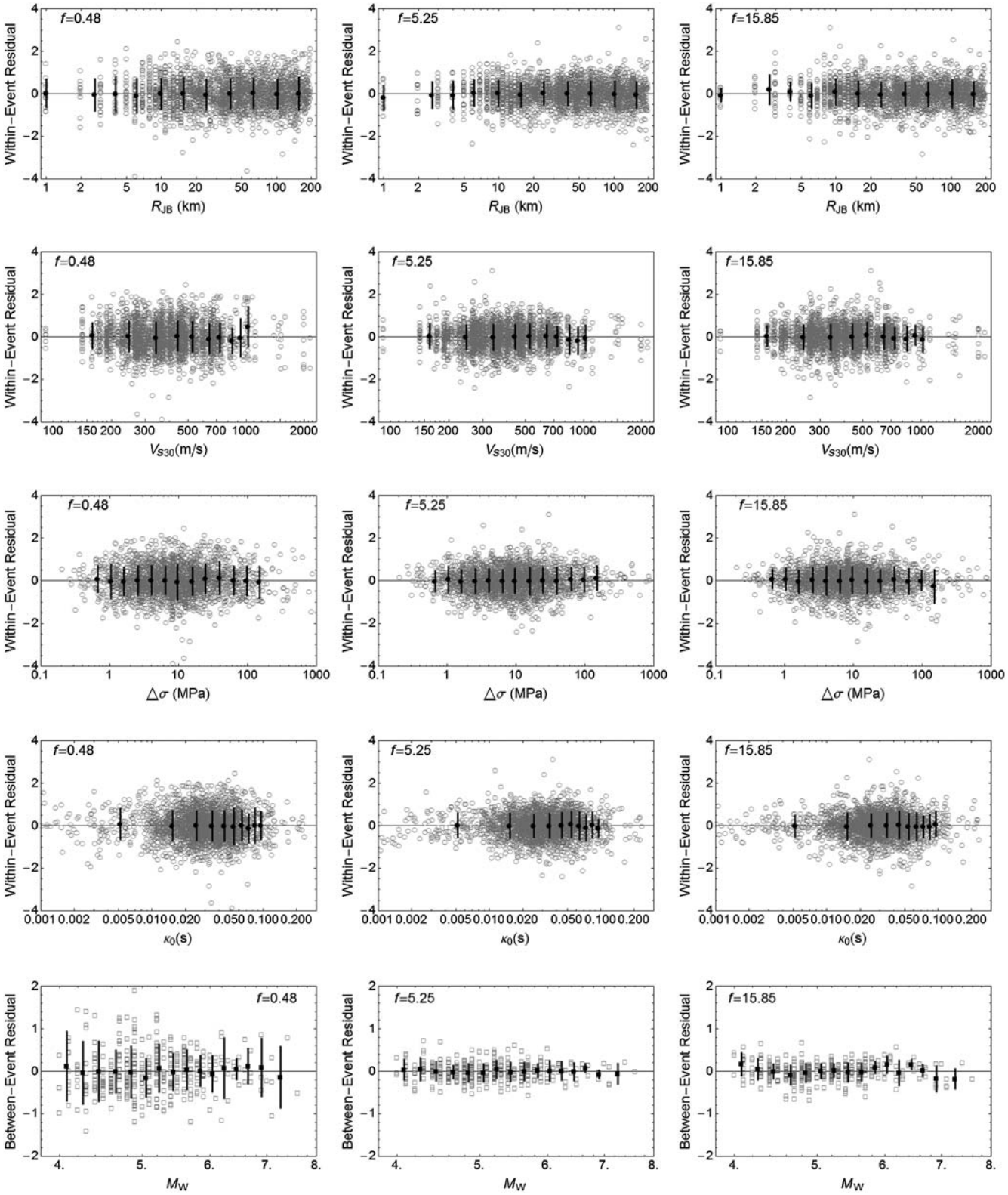

Figure 8. The between-event (open squares) and within-event residuals (open circles) associated with the median FAS model in equation (12) relative to the five predictor variables: moment magnitude (M_w), Joyner–Boore distance (R_{JB}), time-averaged shear-wave velocity in the upper 30 m of the soil column beneath the site (V_{S30}), stress parameter ($\Delta\sigma$), and path-independent high-frequency attenuation (κ_0) at $f = 0.48$, 5.25, and 15.85 Hz. The mean (filled circles) $\pm$ one standard deviation (vertical gray bars) are computed over the bins of width 0.2 (ln units) for distance, 100 m/s for V_{S30}, 0.2 (ln units) for $\Delta\sigma$, and 0.01 (s) for κ_0; only those bins that contain more than 10 records are shown. For between-event residuals, the mean (filled squares) $\pm$ one standard deviation (vertical gray bars) are computed for 0.2-units-wide magnitude bins except the last bin contains all of the earthquakes with $M_w > 7$.

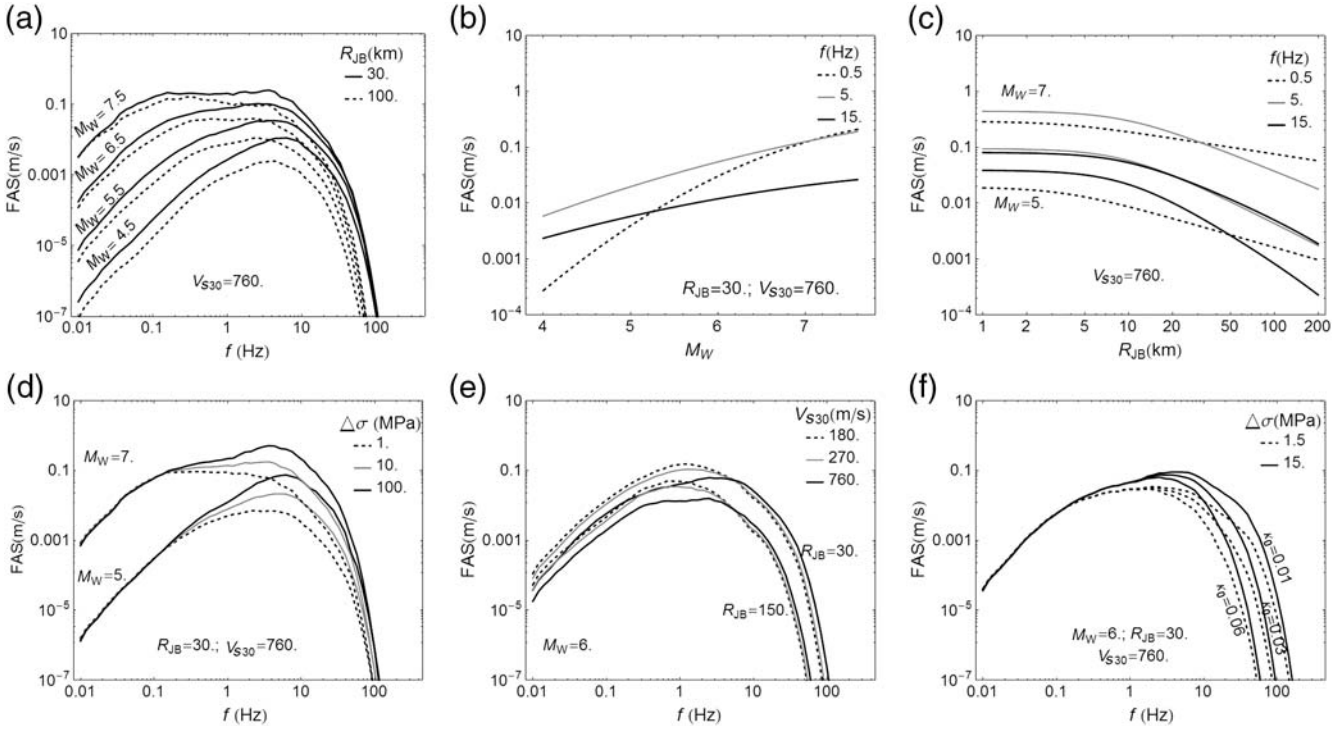

Figure 9. Scaling of (a) the model-predicted FAS with magnitude. (b) spectral amplitudes with M_w, (c) spectral amplitudes with R_{JB}, (d) median FAS with $\Delta\sigma$, (e) V_{S30}, and (f) median FAS with κ_0. For the predictions shown here, the κ_0 values are obtained using equation (7) for corresponding V_{S30} values except for the plots in (f).

duration of ground motion. According to Boore (2003), response spectral ordinate y_{max} at any oscillator frequency f_{osc} is related to the root mean square (rms) motion y_{rms} through a peak factor that is a function of the spectral moments and the duration D_{rvto} as follows:

$$\frac{y_{max}(f_{osc})}{y_{rms}(f_{osc})} = \sqrt{2}\int_0^\infty \{1-[1-\xi\exp(-z^2)]^{N_e}\}dz, \quad (14)$$

in which

$$\xi(f_{osc}) = \frac{m_2}{\sqrt{m_0 m_4}} \quad (15)$$

and the number of extrema N_e is given by

$$N_e(f_{osc}) = \frac{1}{\pi}\sqrt{\frac{m_4}{m_2}}D_{rvto}. \quad (16)$$

The spectral moments (m_k, $k = 0, 2, 4$) at each f_{osc} are computed from the FAS of the response of an SDOF system, which is obtained by multiplying the FAS of the ground motion with the instrument transfer function with 5% damping (equation 7 in Bora *et al.*, 2014). Therefore, to compute D_{rvto} corresponding to an acceleration trace, we treat it as a variable (in the RVT-based response spectrum) to minimize the misfit between the observed and RVT-computed response spectrum. Essentially, a squared mismatch (in log space) is minimized at each oscillator frequency. The other parameter, that is, FAS needed to compute the RVT-based response spectrum, is obtained from the processed records. In the present study, we do not use a different measure of duration, that is, an rms duration (D_{rms}) for computing the y_{rms}. Therefore, the y_{rms} is computed using the zero-th order spectral moment (m_0) and the D_{rvto}:

$$y_{rms}(f_{osc}) = \sqrt{\frac{m_0}{D_{rvto}}}. \quad (17)$$

This differs from Boore (2003), but this approach is possible because of the use of the new optimized value of D_{rvto}. Although D_{rvto} is influenced by the damping (5% in this case) of the SDOF system, it depicts reasonable scaling with commonly used seismological parameters such as magnitude and distance (see the Regression Model for D_{rvto} section). Figure 10 depicts plots of the determined D_{rvto} against the oscillator frequency (left column) for a set of representative scenarios of magnitude and distance. The right column in Figure 10 depicts the closeness of the RVT-optimized and observed response spectra. Often, the response spectral ordinates at oscillator frequencies beyond the cutoff frequencies of the high- and low-pass filters are not considered reliable (Boore and Bommer, 2005), the useable f_{osc} limits were taken as 1.25 and 0.8 times of the cutoff frequencies of the corresponding filters at the low- and high-frequency ends of the Fourier spectra, respectively. Therefore, D_{rvto} was computed only for the useable oscillator frequencies corresponding to the observed response spectrum of a recorded acceleration trace. To

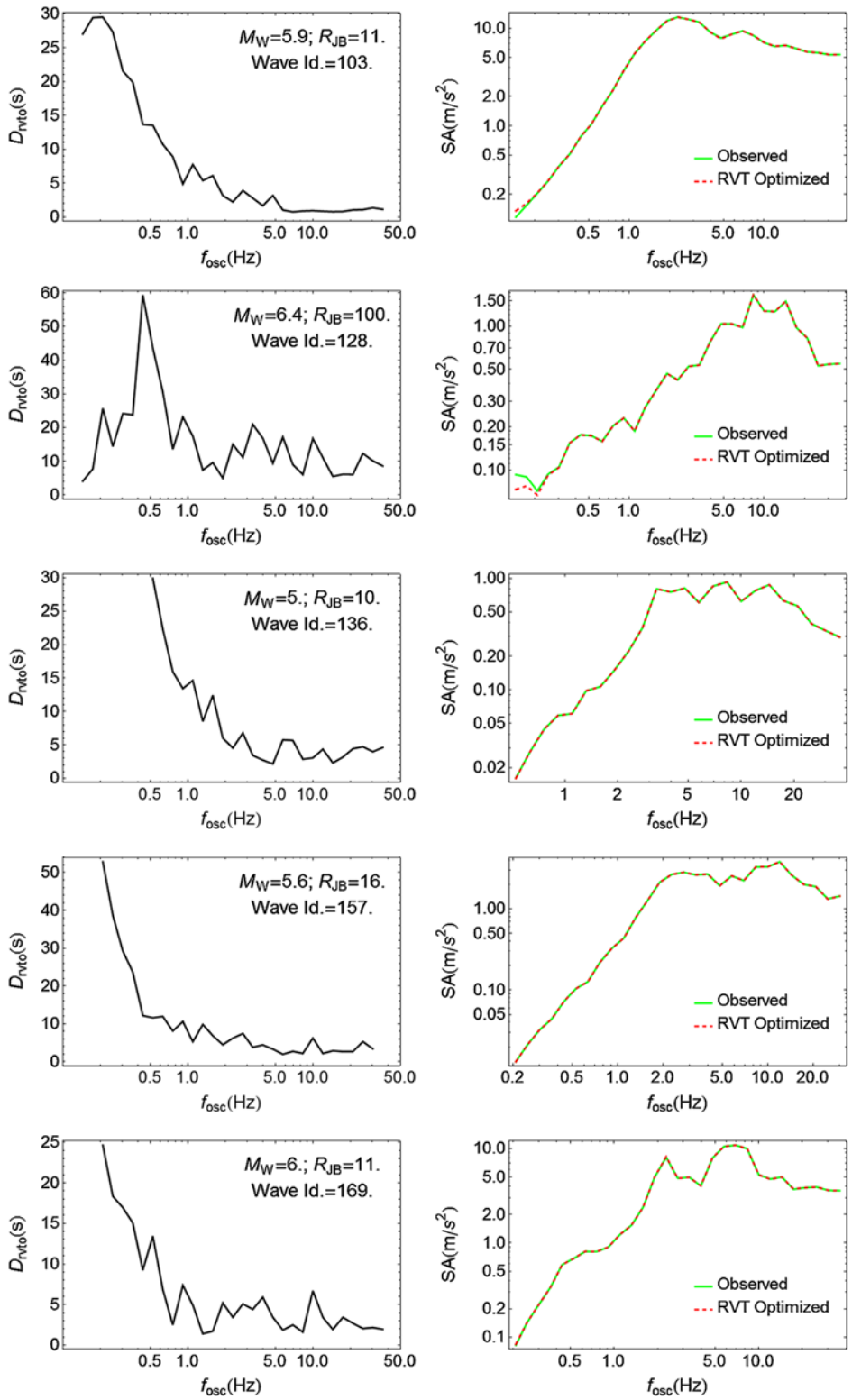

Figure 10. (left) The random vibration theory (RVT) optimized duration (D_{rvto}) compared with oscillator frequency (f_{osc}) for 5% damped single-degree-of-freedom oscillator. (right) The corresponding match between the observed and RVT-based response spectra. The color version of this figure is available only in the electronic edition.

compute D_{rvto} at $f_{osc} = 100$ Hz, the mismatch between the RVT-computed response spectral ordinate (at $f_{osc} = 100$ Hz) and the observed PGA (picked from the time series) was minimized. We further emphasize here that the D_{rvto} values estimated in this way are consistent within the use of the RVT framework and conditioned to the 5% damped SDOF system.

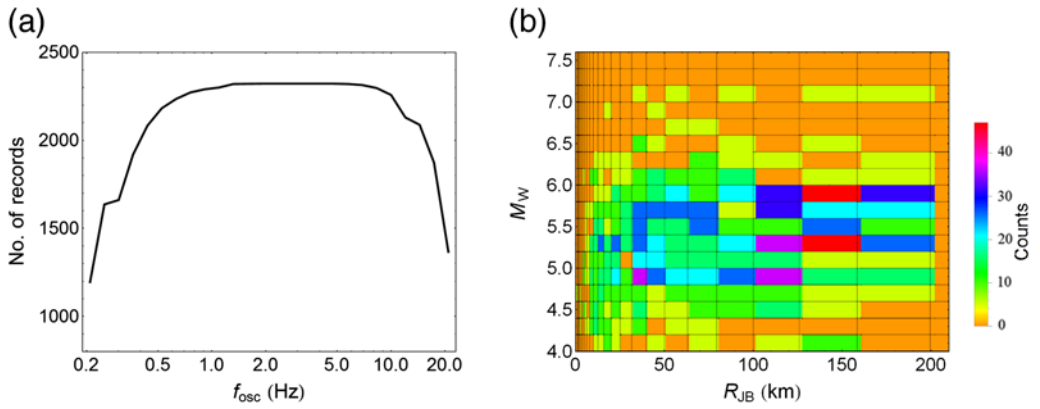

Figure 11. (a) Variation in the number of records available with the selected oscillator frequencies (f_{osc}) for deriving the empirical RVT-optimized duration (D_{rvto}) model. Notice that the records as well as the individual components are considered for regression. (b) Counts in each magnitude–distance bin at $f_{osc} = 1.09$ Hz. The distance (R_{JB}) bins are 0.1 wide in ln units, whereas the magnitude (M_w) bins are 0.2 units wide. The color version of this figure is available only in the electronic edition.

Hence, care should be taken before comparing these values with the other measures of ground-motion duration, for example, significant duration and bracketed duration (Bommer and Martínez-Pereira, 1999). However, as the observed scaling with respect to magnitude and distance indicates, we believe that it represents a combination of several effects on the determined estimate of duration D_{rvto}, including the effect of oscillator response along with the earthquake size, source-to-site distance, and the local site conditions.

Regression Model for Duration (D_{rvto})

Acknowledging the fact that the main objective of this approach of developing a GMPE is to make it adjustable under different seismological conditions, we derive an empirical model for D_{rvto} that allows adjustments for potential ground motions to be easily made. Hence, a functional form similar to that for the empirical FAS model is used in which $\Delta\sigma$ and κ_0 are included as predictor variables in addition to M_w, R_{JB}, and V_{S30}. Inclusion of these additional parameters is motivated by the requirement of consistency with the earlier derived empirical FAS model, which will allow consistent adjustments to be made to both the D_{rvto} and FAS to reflect variations in $\Delta\sigma$ and κ_0. At present, it is difficult to say what the exact dependence of the D_{rvto} over these parameters is supposed to be. The source duration often is assumed to be inversely related to f_c (Boore, 1983, 2003; Boore and Thompson, 2014), so the dependence of D_{rvto} over $\Delta\sigma$ can be considered through the relationship shown in equation (10). We tested different functional forms (additive and multiplicative) for the empirical D_{rvto} model; the selection of the final functional form was derived by the ability of the model to capture the observed scaling of the D_{rvto} along with the one that gives the minimum value of total standard deviation (σ). The functional form, which we adopt for regression, is

$$\ln D_{rvto}(f_{osc}) = d_0 + d_1 M_w + d_2 \ln \Delta\sigma + d_3 \ln \sqrt{R_{JB}^2 + d_4^2} + d_5 \ln V_{S30} + d_6 \ln \kappa_0. \quad (18)$$

The regression was performed on the dataset containing individual horizontal components using equation (18) at each f_{osc} in the 0.21–20.89 Hz range. The definition of predictor variables remains the same as in equation (12). The same random effects algorithm of Abrahamson and Youngs (1992) was performed to decompose the residuals into between-event and within-event terms, which are considered to be lognormally distributed with standard deviation of τ and ϕ, respectively. The total standard deviation was computed using equation (13). Because of the limited useable oscillator-frequency range in the observed response spectra and different useable frequency limits for each record, the number of data points at all the oscillator frequencies were not the same. The variation in the number of data points at each oscillator frequency is depicted in Figure 11a. Figure 11b depicts the number of records in each of the selected magnitude–distance bins at $f_{osc} = 1.09$ Hz. The values of the coefficients involved in equation (18) are listed in Table 2 along with the values of τ, ϕ, and σ.

To check the dependence of the residuals on the predictor variables involved in equation (18), Figure 12 depicts the plot of between-event residuals against magnitude and plot of within-events residuals against distance, V_{S30}, $\Delta\sigma$, and κ_0 at 0.3, 4.79, and 100 Hz. In general, greater dispersion is observed at $f_{osc} = 0.3$ Hz, which gradually decreases at $f_{osc} = 4.79$ and 100 Hz. The larger spread and overprediction in the between-event residuals for $M_w < 5$ at $f_{osc} = 0.3$ Hz can be attributed to the limited dataset used for regression at $f_{osc} < 0.5$ Hz (Fig. 11). Figure 13 depicts the variation of median D_{rvto} with respect to f_{osc} corresponding to all five predictor variables (M_w, R_{JB}, V_{S30}, $\Delta\sigma$, and κ_0) involved in equation (18). In Figure 13, the D_{rvto} values are observed to be higher at low f_{osc} and decreasing toward

Table 2
Coefficients Associated with the Median Prediction of Duration (D_{rvto}) in Equation (18)

f_{osc} (Hz)*	d_0	d_1	d_2	d_3	d_4	d_5	d_6	ϕ*	τ*	σ*
0.21	−0.067	0.647	−0.145	0.372	3.384	−0.203	0.064	0.967	0.617	1.147
0.25	0.553	0.563	−0.167	0.44	3.649	−0.24	0.08	0.968	0.596	1.137
0.30	0.401	0.527	−0.166	0.461	5.857	−0.199	0.074	0.921	0.559	1.077
0.36	1.331	0.414	−0.158	0.41	3.357	−0.213	0.08	0.871	0.569	1.040
0.44	1.507	0.329	−0.142	0.408	4.251	−0.198	0.056	0.841	0.502	0.979
0.53	1.852	0.27	−0.123	0.4	4.572	−0.211	0.069	0.794	0.432	0.904
0.63	2.3	0.181	−0.112	0.426	6.316	−0.218	0.109	0.774	0.408	0.875
0.76	2.987	0.174	−0.118	0.356	5.184	−0.296	0.124	0.735	0.368	0.822
0.91	3.068	0.16	−0.136	0.304	6.07	−0.28	0.12	0.692	0.346	0.774
1.10	2.916	0.152	−0.12	0.319	6.362	−0.292	0.103	0.67	0.3	0.734
1.32	2.73	0.166	−0.112	0.296	4.694	−0.277	0.107	0.615	0.315	0.691
1.59	2.297	0.221	−0.083	0.299	4.77	−0.278	0.119	0.587	0.296	0.657
1.91	2.138	0.222	−0.099	0.33	4.228	−0.274	0.125	0.572	0.3	0.646
2.29	2.13	0.232	−0.095	0.33	4.094	−0.276	0.147	0.543	0.302	0.621
2.75	2.092	0.215	−0.103	0.339	4.429	−0.27	0.152	0.549	0.297	0.624
3.31	2.003	0.252	−0.102	0.37	4.389	−0.307	0.165	0.538	0.301	0.616
3.98	1.602	0.262	−0.111	0.436	6.218	−0.285	0.177	0.517	0.341	0.619
4.79	1.523	0.266	−0.098	0.455	7.057	−0.303	0.165	0.518	0.346	0.623
5.75	1.438	0.282	−0.12	0.483	6.065	−0.313	0.164	0.526	0.346	0.630
6.92	1.216	0.289	−0.135	0.536	7.457	−0.31	0.169	0.507	0.375	0.631
8.32	0.706	0.288	−0.124	0.586	7.632	−0.272	0.148	0.493	0.367	0.615
10.00	0.241	0.306	−0.113	0.593	7.266	−0.238	0.113	0.498	0.347	0.607
12.02	0.372	0.297	−0.12	0.615	6.951	−0.271	0.103	0.504	0.375	0.628
14.45	0.6	0.291	−0.121	0.614	6.579	−0.309	0.092	0.511	0.389	0.642
17.38	0.358	0.311	−0.124	0.613	6.567	−0.291	0.084	0.515	0.405	0.655
20.89	0.284	0.337	−0.125	0.59	6.887	−0.311	0.065	0.508	0.433	0.667
100.	1.266	0.372	−0.123	0.522	5.53	−0.443	0.127	0.514	0.388	0.644

*f_{osc}, oscillator frequency; ϕ, within-event standard deviation; τ, between-event standard deviation; σ, total standard deviation.

higher f_{osc}. There can be several effects that control such a behavior such as the effect of the oscillator response in which the damping of the oscillator can have strong influence. However, for the damping that is used in this study (i.e., 5% critical damping), it can also be observed that seismological parameters like earthquake size (Fig. 13a) and source-to-site distance (Fig. 13b) also influence the D_{rvto}, with the greatest effects seen for low f_{osc}. The parameter V_{S30} (Fig. 13c) is found to affect the D_{rvto} estimates mainly at low f_{osc}, though for a large difference in V_{S30} (e.g., 180 and 760 m/s) a significant difference at high f_{osc} is also observed. Similarly, $\Delta\sigma$ (Fig. 13d) and κ_0 (Fig. 13e) are observed to affect the D_{rvto} more at low f_{osc} than at higher f_{osc}. It appears from Figure 13 that the $\Delta\sigma$ is the most significant parameter after magnitude and distance in influencing D_{rvto}, which one might expect assuming its dependence upon $\Delta\sigma$ through the f_c using equation (10).

Response Spectra

We compute the response spectrum using a combination of the empirical FAS model (equation 12) and the empirical D_{rvto} model (equation 18). Essentially, equations (14)–(17) are used to obtain the forward predictions of response spectra using the two empirical models of FAS and D_{rvto}. As noted earlier, the empirical D_{rvto} model is derived for the oscillator frequencies in the 0.21–20.89 Hz range and for PGA, that is, $f_{osc} = 100$ Hz. For having the D_{rvto} estimates at $f_{osc} < 0.21$ and $20.89 < f_{osc} < 100$ Hz, the (D_{rvto}) values corresponding to 0.21 and 20.89 Hz are considered, respectively. However, a careful evaluation of the between-event residuals for D_{rvto} and the response spectral ordinate at $f_{osc} = 100$ Hz indicate a strong correlation between the two. The observed general trend indicates that an increase (or decrease) in the actual D_{rvto} by a certain factor will lead to the corresponding decrease (or increase) in the response spectral ordinates by the same factor. The response spectral comparisons depicted in Figure 12 of our previous article (Bora *et al.*, 2014) indicated a consistent underprediction at high f_{osc}, for which median predictions of empirical FAS and the D_{gm} model were used to obtain the response spectral ordinates. To mitigate this behavior, we opted to use the mean values of FAS, that is, $Y(f)$ predictions in the present study with the rationale that it represents the expected value of FAS for a given scenario. However, the Fourier spectral ordinates cannot be considered as independent from one another. In the present study, for obtaining the final median response spectral ordinates, we tested four combinations of predicted FAS and D_{rvto} in terms of mean and median values. It was observed that the combination of mean FAS and mean D_{rvto} values gives the minimum bias and variance

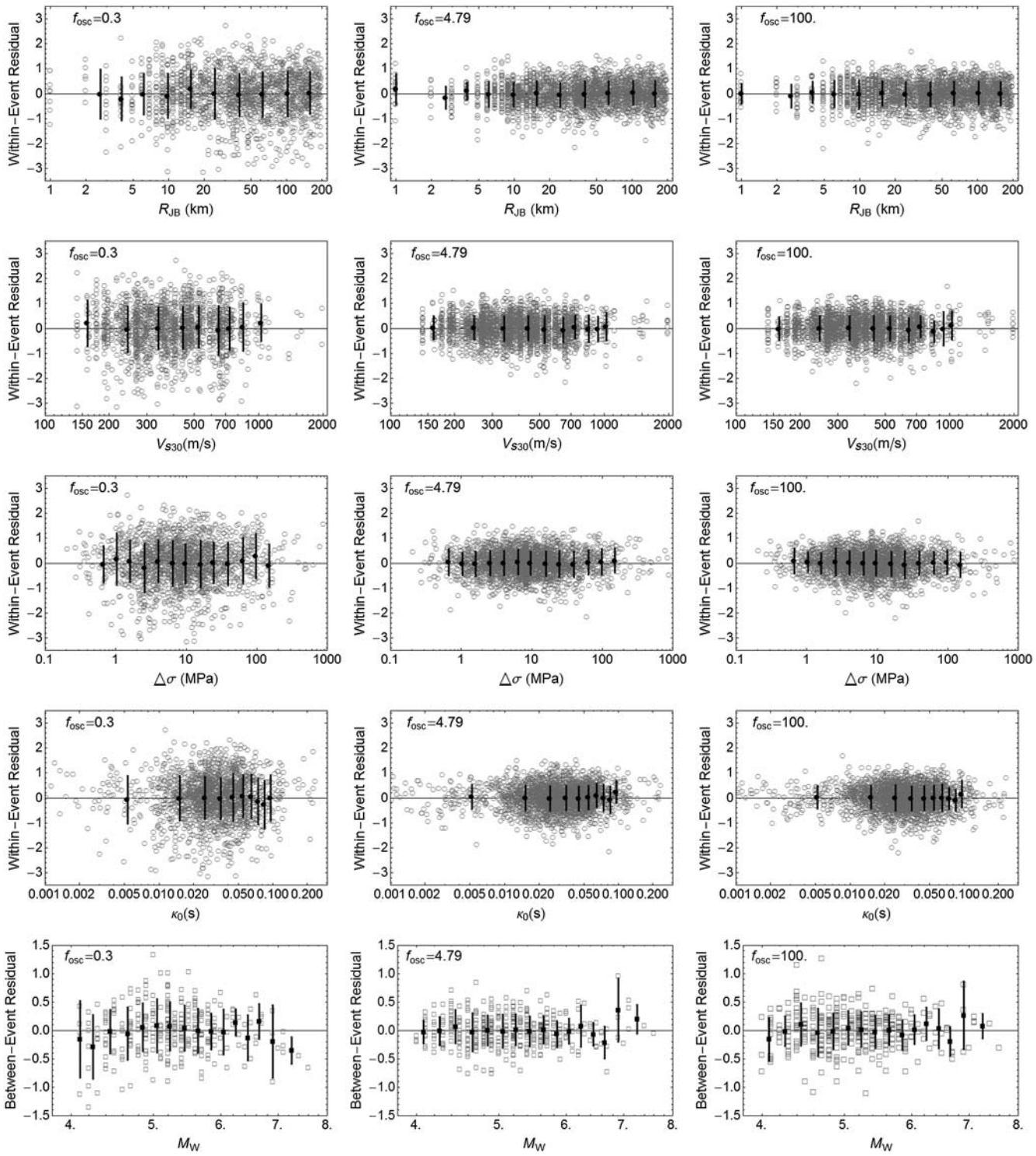

Figure 12. Between-event (open squares) and within-event residuals (open circles) associated with the median D_{rvto} model in equation (18) compared with the five predictor variables: M_w, R_{JB}, V_{S30}, $\Delta\sigma$, and κ_0 at $f_{osc} = 0.3$, 4.79, and 100 Hz. The mean (filled circles) ± one standard deviation (vertical gray bars) are computed over the bins of width 0.2 (ln units) for distance, 100 m/s for V_{S30}, 0.2 (ln units) for $\Delta\sigma$, 0.01 (s) for κ_0; only those bins are shown which contain more than 10 records. For between-event residuals, the mean (filled squares) ± one standard deviation (vertical gray bars) are computed for 0.2 wide magnitude bins except the last bin contains all of the earthquakes with $M_w > 7$.

of response spectral ordinates using the present approach and empirical equations presented in this study. Hence, to obtain the median response spectral presented in this study, we use mean values of both FAS and D_{rvto} predictions. A point worth emphasizing is that the difference between median and mean of FAS and D_{rvto} should be noted. The regression models in equations (12) and (18) utilize the natural logarithm of $Y(f)$ and that of $D_{rvto}(f_{osc})$, assuming that they are lognormally

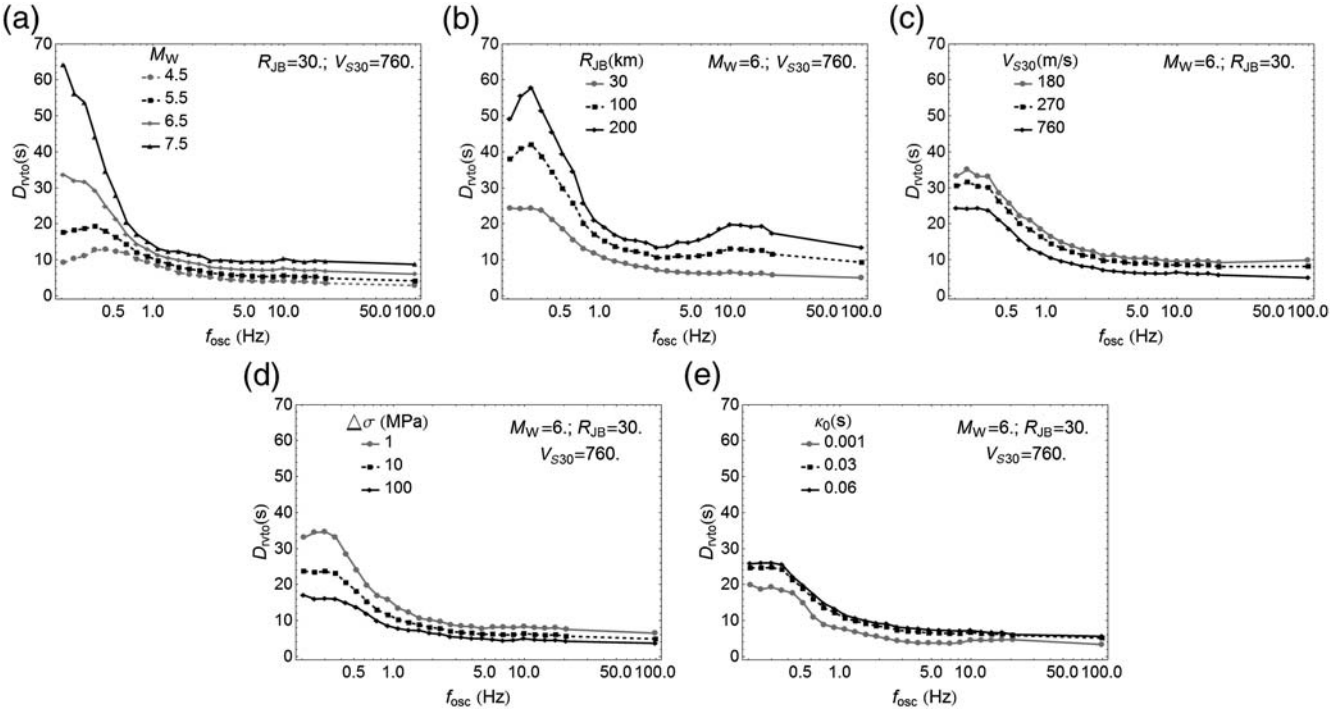

Figure 13. The variation of predicted median D_{rvto} compared with f_{osc} with scaling with respect to (a) M_{w}, (b) R_{JB}, (c) V_{S30}, (d) $\Delta\sigma$, and (e) κ_0.

distributed. Therefore, for a particular scenario of predictor variables, equations (12) and (18) give the mean of $\ln Y(f)$ and that of $\ln D_{\mathrm{rvto}}(f_{\mathrm{osc}})$, respectively. The two essentially represent the median values of their respective linear probability density functions, that is, $Y(f)$ and $D_{\mathrm{rvto}}(f_{\mathrm{osc}})$. The mean value of $Y(f)$ can be obtained using the mean $\ln Y(f)$ and associated total uncertainty σ (in ln units). Similarly, the mean value of $D_{\mathrm{rvto}}(f_{\mathrm{osc}})$ can also be computed using mean $\ln D_{\mathrm{rvto}}(f_{\mathrm{osc}})$ and corresponding σ.

As a consistency check, a comparison is performed (in terms of median predictions) between the presented analysis and other GMPEs that have been developed using the same database (RESORCE). Only the GMPEs of Akkar, Sandıkkaya, and Bommer (2014), Bindi *et al.* (2014), and Bora *et al.* (2014) are considered for comparison, because they involve a parametric functional form in their regression analysis. Comparison among the median GMPEs was performed for the same scenarios of magnitude, distance, and V_{S30}, which have been used in Douglas *et al.* (2014). It is worth noting that Douglas *et al.* (2014) uses the comparison paper of Abrahamson *et al.* (2008) as a template; hence a comparison between the figures presented here can also be made to those shown in Abrahamson *et al.* (2008) and the recently published Next Generation Attenuation-West 2 (NGA-West 2) models of Gregor *et al.* (2014). Moreover, the GMPE of Boore *et al.* (2014) is also used, which is expected to facilitate a comparison between our approach and NGA-West 2 models (Bozorgnia *et al.*, 2014). This NGA model was chosen because it utilizes R_{JB} as the distance metric. Ⓔ For the figures depicting the comparison among the aforementioned empirical models in terms of median predictions of response spectral ordinates, see Figures S1–S7.

Distance Scaling

Ⓔ The attenuation with distance for PGA and 1 Hz spectral amplitude with 5% damping is presented in Figure S1. Figure S1 depicts the comparison for $V_{S30} = 760$ m/s and Figure S2 depicts the same comparison for $V_{S30} = 270$ m/s. We consider 100 Hz spectral amplitude as the PGA from our approach. To predict the response spectral values using our approach along with the median $\Delta\sigma = 8.4$ MPa (the average value associated with the dataset), the κ_0 values 0.024 and 0.031 s (obtained from equation 7) are used, corresponding to $V_{S30} = 760$ and 270 m/s, respectively. The dataset we used for deriving the GMPEs does not contain recordings from any earthquake beyond magnitude 7.6. Nevertheless, for consistency in comparing the predictions with the other GMPEs, we also show predictions for $M_{\mathrm{w}} = 8$. The shape of the distance scaling presented in this study is similar to the other models considered here. A slower decay rate with distance can be observed toward the larger-magnitude events. For PGA, the decay rate presented from our approach is observed to be similar to the decay rate predicted by Akkar, Sandıkkaya, and Bommer (2014) and Bindi *et al.* (2014); however, it is faster than predicted by Boore *et al.* (2014). For the 1 Hz spectral amplitude, our approach predicts a slightly slower decay rate in comparison to the other two RESORCE GMPEs.

Magnitude Scaling

Ⓔ Scaling of PGA and spectral amplitudes at $f_{osc} = 0.33$, 1, and 5 Hz is shown in Figure S3. The nonlinear magnitude scaling of spectral amplitudes with larger magnitude is readily visible. Overall, the magnitude scaling obtained from our approach is in good agreement with that from other GMPEs. The PGA values predicted from the present study and those by Akkar, Sandıkkaya, and Bommer (2014) and Bindi *et al.* (2014) are similar. However, toward low f_{osc}, the values presented from our approach are slightly higher at $f_{osc} = 0.3$ and 1 Hz. The consistently higher values with respect to the values obtained in Bora *et al.* (2014) are because of the use of mean FAS in this study.

Scaling with V_{S30}

Ⓔ The scaling of response spectral ordinates with V_{S30} is depicted in Figure S4. Though, it is difficult to constrain the nonlinear soil response empirically with the given dataset, in which most of the records correspond to low-to-moderate magnitudes, the effect of nonlinear site response at short distances and high f_{osc} on soil sites cannot be ignored. However, the broad trend that can be observed from Figure S4 is that the low V_{S30} values give rise to higher spectral amplitudes and vice versa. It can be easily observed from Figure S4a,b that the scaling of response spectral ordinates with V_{S30} predicted from the present study indicates an overall good agreement in the linear domain of the site response with the other RESORCE GMPEs at both $R_{JB} = 100$ and 10 km. It should be noticed that the $V_{S30} - \kappa_0$ relationship given in equation (7) is used to obtain the κ_0 values corresponding to different V_{S30} values shown in the comparison.

Ⓔ Figure S5 shows the variation of the ratio of spectral amplitudes on sites with V_{S30} of 270 and 760 m/s at different oscillator frequencies for two different distances of $R_{JB} = 10$ and 100 km (left panels) and for sites with V_{S30} values of 490 and 760 m/s (right panels). From Figure S5, the ratio of spectral amplitudes predicted from the present study is found to be in good agreement with those obtained from other RESORCE GMPEs, including the model of Boore *et al.* (2014). However, the ratio of the spectral amplitudes between soil and rock sites from the present study is lower than the other GMPEs at $R_{JB} = 100$ km, where the ratio of spectral amplitudes between V_{S30} 270 and 760 ranges from 2 to 3.

Predicted Response Spectra

The Ⓔ predicted response spectra for $M_w = 5$, 6, 7, and 8 at $R_{JB} = 10$ km corresponding to $V_{S30} = 760$ m/s are depicted in Figure S6. In general, the response spectral values obtained by our model are in good agreement with the other models. Similarly, Ⓔ Figure S7 depicts the response spectra for $M_w = 7$ at $R_{JB} = 10$ km corresponding to $V_{S30} = 270$ and 760 m/s. The values from our model for low $V_{S30} = 270$ m/s are also in good agreement with the other models.

In addition, we depict the Ⓔ scaling of response spectra with $\Delta\sigma$ and κ_0 in Figure S8. Figure S8 depicts the $\Delta\sigma$ scaling of response spectra for different magnitudes corresponding to $V_{S30} = 760$ m/s. The $\Delta\sigma$ is observed to affect the high oscillator frequency amplitudes, increasing the spectral level with increasing $\Delta\sigma$. The low oscillator frequency spectral amplitudes are almost unaffected by the change in the $\Delta\sigma$ which are completely determined by the magnitude. Figure S8 depicts the scaling with respect to κ_0 for different $\Delta\sigma$ values. It can easily be seen that the high-frequency response spectral amplitudes are completely determined by the $\Delta\sigma$ and κ_0 for a fixed magnitude, distance, and V_{S30} scenario. The $\Delta\sigma$ is seen to affect the spectral amplitudes at $f_{osc} > 0.3$ Hz, whereas κ_0 influences the spectral amplitudes beyond 2 Hz.

Variability in Response Spectra

Finally, an estimate of the aleatory variability involved in the predicted response spectra using the present analysis is performed. For this purpose, the response spectral residuals are computed; and, for obtaining the residuals at each f_{osc}, the log (natural) of the predicted spectral amplitudes are subtracted from the log (natural) of the observed corresponding spectral amplitudes. The predicted spectral amplitudes are obtained by combining the predictions from FAS and D_{rvto} models through RVT. Subsequently, the residuals are partitioned into between-event and within-event components using the algorithm suggested by Abrahamson and Youngs (1992). In Figure 14, both the residuals at $f_{osc} = 0.3$, 5, and 100 Hz are plotted against all five predictor variables used in the empirical models for FAS and D_{rvto}. Although, the residuals have not been computed as the outcome of a standard regression procedure, a stable variation of the residuals around zero can be observed. The scatter among the residuals is larger toward the low oscillator frequencies in comparison to the high frequencies. For between-event residuals, the scatter is larger at $f_{osc} = 0.3$ Hz, and a slight overprediction is also observed. This trend in between-event residuals at $f_{osc} = 0.3$ Hz can be due to the fact that the D_{rvto} model is not well constrained at $f_{osc} < 0.5$ Hz. Although, the style-of-faulting was not included as a predictor variable in our empirical models for FAS and D_{rvto}, the residuals are depicted for the three styles of faulting in Figure 15. Overall there is no trend observed except at $f_{osc} = 0.3$ Hz, where an overprediction is indicated.

Figure 16 depicts the variation of aleatory variability in terms of between-event (τ), within-event (ϕ), and total (σ) standard deviation against f_{osc}, respectively. For comparison in Figure 16, the τ, ϕ, and σ values corresponding to $M_w \geq 5.5$, $R_{JB} < 80$, and $V_{S30} > 300$ m/s of Boore *et al.* (2014) are used. One of the technical hurdles associated with our earlier presented model in Bora *et al.* (2014) was the high values of total standard deviation. One of the notable achievements of this study that can be observed in Figure 16 is that we obtained a significant reduction in all three standard deviation values at high oscillator frequencies. The most

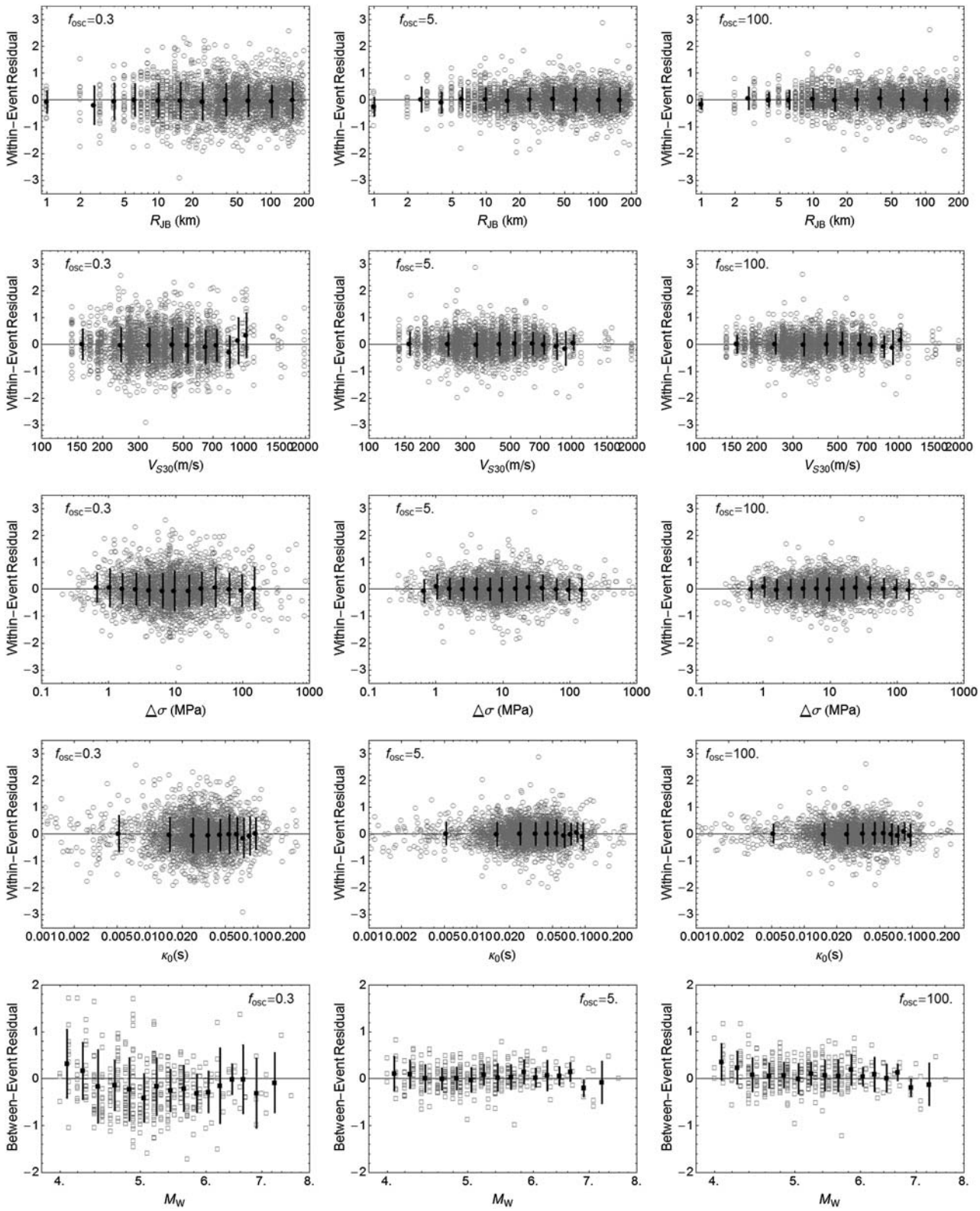

Figure 14. Within-event (open circles) and between-event (open squares) response spectral residuals compared with M_w, R_{JB}, V_{S30}, $\Delta\sigma$, and κ_0 at $f_{osc} = 0.3$, 5, and 100 Hz. The residuals are computed by subtracting the natural logarithm of response spectral ordinates obtained as a combination of FAS and D_{rvto} models (through RVT) from the natural logarithm of the observed response spectral ordinates. The mean (filled circles) $\pm$ one standard deviation (vertical gray bars) are computed over the bins of width 0.2 (ln units) for distance, 100 m/s for V_{S30}, and 0.2 (ln units) for $\Delta\sigma$, 0.01 (s) for κ_0; only those bins that contain more than 10 records are shown. For between-event residuals the mean (filled squares) $\pm$ one standard deviation (vertical gray bars) are computed for 0.2-unit-wide magnitude bins, except the last bin contains all of the earthquakes with $M_w > 7$.

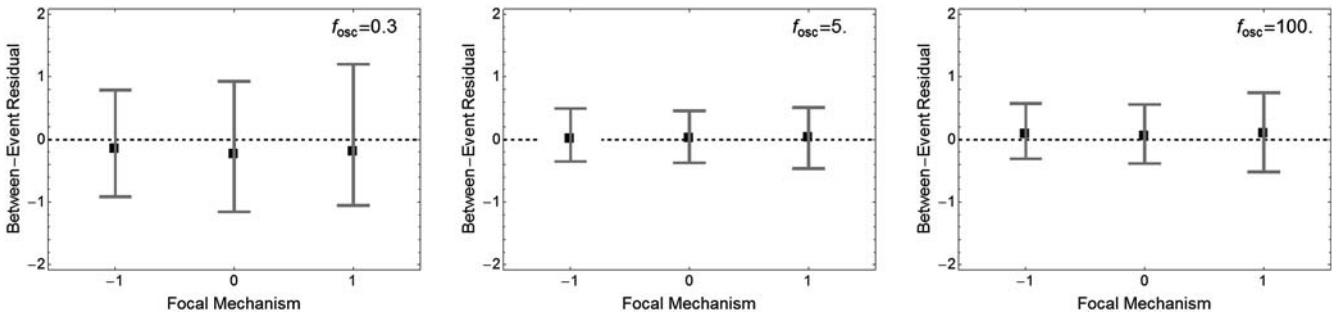

Figure 15. The mean (filled squares) ± one standard deviation (vertical gray bars) of between-event residuals compared with the style of faulting, in which −1, 0, and 1 represent normal, strike slip, and reverse faulting, respectively.

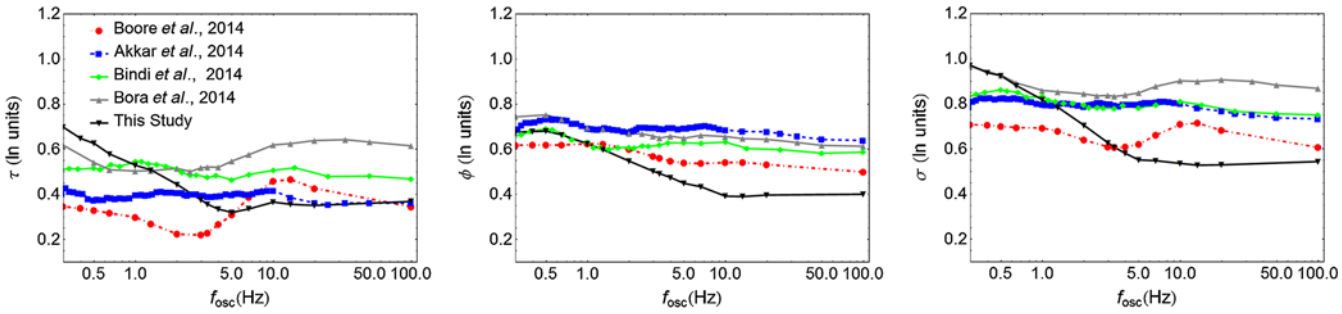

Figure 16. Comparison among the five empirical response spectral models in terms of between-event (τ), within-event (ϕ), and total standard deviation (σ). The standard deviation terms from Boore *et al.* (2014) are computed for M_w 5.5, R_{JB} = 10 km, and V_{S30} > 760 m/s. The color version of this figure is available only in the electronic edition.

striking feature that can be observed is the total standard deviation beyond $f_{osc} = 2.5$ is lower by a factor of 1.5 in comparison to the models of Akkar, Sandıkkaya, and Bommer (2014) and Bindi *et al.* (2014). The values of total standard deviation (σ) are also found to be lower than those of Boore *et al.* (2014) at high frequencies; however, a major part of this reduction obtained in σ is due to the approach we used here for the development of the response spectral GMPE, in which the record-specific $\Delta\sigma$ and κ_0 parameters are used. In light of this point, the reduction in σ obtained by the approach presented herein is unlikely to reflect the true variability for the typically given scenarios of event-specific $\Delta\sigma$ and station-specific κ_0 parameters; the residuals were also computed using the event-specific $\Delta\sigma$ and station-specific κ_0 parameters. The event-specific $\Delta\sigma$ was computed as the median over all the records originated from the given earthquake; similarly station-specific κ_0 was computed as the median over all the records obtained at a given station. In addition to that, the database average values of $\Delta\sigma$ (median = 8.4 MPa) and κ_0 (median = 0.03 s) parameters were also used to compute the residuals. Figure 17 depicts the variation of τ, ϕ, and σ for these two cases with respect to f_{osc}, along with the comparison with those of the Akkar, Sandıkkaya, and Bommer (2014) GMPE. Although the τ and σ values with the database-average values of $\Delta\sigma$ and κ_0 parameters are higher than those of Akkar, Sandıkkaya, and Bommer (2014), the corresponding values are considerably lower, using the event-specific and station-specific values of the $\Delta\sigma$ and κ_0 parameters.

Guidelines for Using the Present GMPE

The presented approach of developing a response spectral GMPE that provides options for adjusting the response spectral ordinates to different seismological conditions is derived using the two separate empirical models for FAS and D_{rvto} of ground motion combined within the RVT framework. The empirical models were derived for an average horizontal component using individual record components in the regression. Based upon the predictor variable range in the selected dataset, the present empirical models are considered to be applicable in the magnitude range $4 \le M_w \le 7.6$ at $R_{JB} \le 200$ km. Though the station V_{S30} values in the given dataset range from 92 to 2165 m/s, the present GMPE should be considered well constrained in the V_{S30} range 160–1030 m/s, corresponding to 2% and 98% quantiles of the dataset, respectively. Similarly, the applicable $\Delta\sigma$ and κ_0 ranges are 0.8–138 MPa and 0.003–0.1 s, respectively. Moreover, the empirical FAS model derived herein does not account for a nonlinear site behavior that can be significant at soft soil sites experiencing strong shaking. Therefore, a calibration of high oscillator frequency response spectral ordinates with the observed data and other GMPEs at sites corresponding to loose soils and shorter distances is sug-

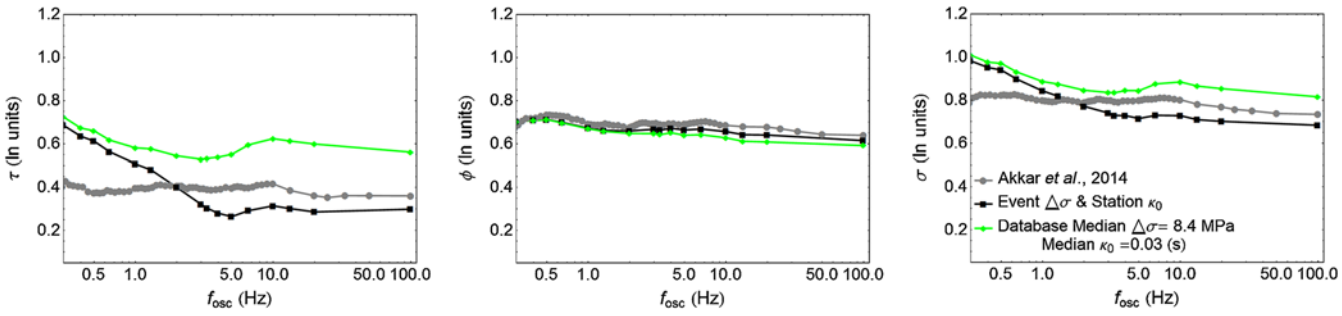

Figure 17. The variation of τ, ϕ, and σ for average values of $\Delta\sigma$ and κ_0 parameter. For the computation of the residuals, the event-specific $\Delta\sigma$ and station-specific κ_0 are computed as the median values of respective record-specific values assuming a lognormal distribution. The color version of this figure is available only in the electronic edition.

gested before applying the present GMPE. In addition to that, based upon the method used to develop the present method of deriving the response spectral GMPE, we suggest certain guidelines for using the results presented in this article. As noted previously, we use the peak factor of Cartwright and Longuet-Higgins (1956) to relate the y_{max} and y_{rms}. A different definition of this peak factor is expected to affect the estimates of D_{rvto} from an observed accelerogram and likewise for making forward predictions of response spectra using the two empirical models. Hence, for having a consistent estimate of response spectral ordinates, the use of the same peak factor is suggested. The D_{rvto} is computed with the assumption $D_{rms} = D_{rvto}$, therefore the same relationship is required for making forward predictions of response spectral ordinates using the present approach. Moreover, the D_{rvto} estimates are determined for 5% damping of the SDOF system; consequently, the empirical D_{rvto} model derived herein should be considered valid with 5% damping of the oscillator. The low values of aleatory variability obtained are consistent with the methodological framework presented in this study. The use of record-specific values for $\Delta\sigma$ and κ_0 parameters gave very small values of the total uncertainty σ. A better representation of the true decrease in uncertainty due to the inclusion of the $\Delta\sigma$ and κ_0 can be obtained if commonly used event-specific and site-specific values are used for them. Therefore, for the scenarios of event-specific $\Delta\sigma$ and station-specific κ_0 parameters or database-averaged values of these parameters, the values of the total standard deviation given in Figure 17 should be used. In addition to that, as mentioned previously, the results presented in this study are obtained for the mean values of predicted FAS and D_{rvto}. Although Fourier spectral amplitudes are often considered as correlated, this decision was based upon the low values of variance (of median response spectra) obtained for this combination. Though one can use the median value of the FAS and D_{rvto} empirical models as well, we observed an underprediction as compared to other regional models using the median values for FAS and D_{gm} models in our previous article (Bora *et al.*, 2014, see fig. 12).

Conclusions

This article presents a complete framework for developing a full response spectral GMPE that is easily adjustable to account for differences in source, path, and site condition effects. Similar to the approach described in Bora *et al.* (2014), it utilizes the RVT to combine the empirical models for FAS and D_{rvto}. This study supersedes our previous model in Bora *et al.* (2014). With the increased usage of the single-station sigma concept (Atkinson, 2006; Rodriguez-Marek *et al.*, 2014), the present approach provides a physically consistent, transparent, and easy-to-implement framework for adjusting a median response spectral GMPE. Moreover, the present approach can also be used to compute the adjustment factors for other similar response spectral GMPEs that are used to construct the logic tree for the median ground-motion model in a site-specific PSHA study, as described in Bommer *et al.* (2014) for Thyspunt, a new build nuclear site in South Africa.

The extended frequency range of the empirical FAS model as compared to the previous FAS model in Bora *et al.* (2014) facilitates making adjustments at high f_{osc} even for very low κ_0 values. The frequency range of the empirical model was extended by stochastic model parameters determined from the observed acceleration traces. This modeling of the acceleration trace in terms of stochastic model predictions comes with the strong assumption that the FAS can be represented by a far-field spectrum. Essentially, this permits us to model the source in terms of the point-source model (Brune, 1970) with a simple geometrical spreading and anelastic attenuation models which may not be appropriate for $M_w > 6.5$ earthquakes. However, such models are often used in simulating ground motions with the stochastic modeling approach (Boore, 2003) and have been found to be successful in predicting peak ground motions of engineering interest. Though, it is useful to test the validity of such approaches, in this study most of the events have $M_w < 6.5$, and additionally records with hypocentral distance $R > 30$ km corresponding to $M_w \geq 6.5$ earthquakes have been discarded to enable the aforementioned point-source approximation. Though, the stochastic model parameters determined from the selected dataset

should be tested and corroborated with those determined from different and independent analyses, the goal of the present study was to derive a response spectral GMPE rather than to determine the robust stochastic model parameter estimates. Therefore, the use of the stochastic model and determination of some of its parameters (i.e., record-specific $\Delta\sigma$ and κ_0) should be considered in this context.

Though the median ground motion predicted by the present approach should be consistent with the range of the predictor variable values, the use of record-specific values for $\Delta\sigma$ and κ_0 overestimates the reduction in the total variability. Therefore, a better representation of variability can be obtained with the often used event-specific $\Delta\sigma$ and station-specific κ_0 values. Nevertheless, the present approach aims to provide a physically consistent and transparent method to adjust the median ground motions within the framework of a single-station sigma (Rodriguez-Marek *et al.*, 2014) in which the sigma model is constructed separately; because the adjustments made in the GMPE are expected to introduce additional epistemic uncertainties.

A different measure of duration in terms of D_{rvto} is suggested for which the empirical model was derived. The present measure of D_{rvto} should be considered consistent within the use of RVT to obtain the response spectral ordinates. The selection of the functional form for the empirical D_{rvto} model was primarily derived by the ability of the model to capture the observed scaling of D_{rvto} with respect to the predictor variables such as magnitude, distance, and V_{S30} along with the lowest associated uncertainty in the predicted D_{rvto}. The $\Delta\sigma$ and κ_0 are included in the D_{rvto} empirical model to obtain the adjustments in the median D_{rvto} consistent with the adjustments in median FAS. However, the physical explanation for D_{rvto} and its dependence upon the seismological parameters such as magnitude, distance, V_{S30}, $\Delta\sigma$, and κ_0 still needs to be further investigated with the use of different datasets along with the simulations, which can also provide crucial guidance.

The coherency of the present approach with other classical response spectral GMPEs was tested by performing graphical comparisons in terms of median predictions. For comparison, other RESORCE GMPEs of Akkar, Sandıkkaya, and Bommer (2014), Bindi *et al.* (2014), and Bora *et al.* (2014), along with one representative NGA GMPE of Boore *et al.* (2014), were considered. Though the uncertainties associated with the present response spectral GMPE were found to be considerably lower than that of other GMPEs, the median response spectral ordinates obtained from the present approach were reasonably comparable with those of other classical response spectral GMPEs. It must again be emphasized that the present response spectral GMPE does not involve a term to model nonlinear site response. However, such effects in high oscillator frequency response cannot be ignored at short distances from large-magnitude events.

Given the consistency of the presented approach with the classical regression-based response spectral GMPEs, this study paves the path for using empirical Fourier models in studies related with seismic-hazard analysis. We believe that the success of empirical FAS models does not lie only in its ability to model the ground motions in a physically consistent manner but also in that it can be useful in assessing the epistemic uncertainty in terms of the contributions from different attributes of ground motion such as source, path, and site. Epistemic uncertainty can also be captured using appropriate combinations of $\Delta\sigma$ and κ_0 in the present GMPE within the logic-tree framework. Possibilities for further improvements, particularly with respect to the duration model (with its physical explanation) in the present approach can be explored with the use of different datasets such as the NGA and Japanese datasets (Okada *et al.*, 2014).

Data and Resources

The present analysis is performed on the RESORCE-2012 database (Akkar, Sandıkkaya, Şenyurt, *et al.*, 2014), which is compiled within the framework of the Seismic Ground-Motion Assessment (SIGMA) project. The entire analysis that is presented in this article was carried out by implementing various routines and subroutines in the programming software Mathematica (http://www.wolfram.com/mathematica/; last accessed April 2015).

Acknowledgments

Sanjay Singh Bora is grateful to the Helmholtz Research School GeoSim for providing a fellowship. This research was partly funded by the Seismic Ground-Motion Assessment (SIGMA) project. Benjamin Edwards is thankful to the Swiss Federal Nuclear Safety Inspectorate for providing funds for his contribution in the present study. The authors appreciate and thank Fabrice Cotton for stimulating discussions and feedback provided by him at various stages of the present study. The authors would also like to thank Pierre-Yves Bard for his comments and suggestions. Christian Molkenthin and Olga Ktenidou are also thanked for their feedback, which led to improvements of the presented analysis. We are also grateful to the two anonymous reviewers for their comments and suggestions, which contributed significantly to bring the manuscript in its present form.

References

Abrahamson, N. A., and R. R. Youngs (1992). A stable algorithm for regression analyses using the random effects model, *Bull. Seismol. Soc. Am.* **82,** no. 1, 505–510.

Abrahamson, N., G. Atkinson, D. Boore, Y. Bozorgnia, K. Campbell, B. Chiou, I. M. Idriss, W. Silva, and R. Youngs (2008). Comparisons of the NGA ground-motion relations, *Earthq. Spectra* **24,** no. 1, 45–66.

Akkar, S., M. A. Sandıkkaya, and J. J. Bommer (2014). Empirical ground-motion models for point- and extended-source crustal earthquake scenarios in Europe and the Middle East, *Bull. Earthq. Eng.* **12,** no. 1, 359–387.

Akkar, S., M. A. Sandıkkaya, M. Şenyurt, A. A. Sisi, B. Ö. Ay, P. Traversa, J. Douglas, F. Cotton, L. Luzi, B. Hernandez, *et al.* (2014). Reference database for seismic ground-motion in Europe (RESORCE), *Bull. Earthq. Eng.* **12,** 311–339.

Anderson, J. G., and S. E. Hough (1984). A model for the shape of the Fourier amplitude spectrum of acceleration at high frequencies, *Bull. Seismol. Soc. Am.* **74,** no. 5, 1969–1993.

Atkinson, G. M. (1993). Notes on ground-motion parameters for eastern North America: Duration and H/V ratio, *Bull. Seismol. Soc. Am.* **83,** no. 2, 587–596.

Atkinson, G. M. (2004). Empirical attenuation of ground-motion spectral amplitudes in southeastern Canada and the northeastern United States, *Bull. Seismol. Soc. Am.* **94,** no. 6, 2419–2423.

Atkinson, G. M. (2006). Single-station sigma, *Bull. Seismol. Soc. Am.* **96,** no. 2, 446–455.

Atkinson, G. M., and I. Beresnev (1997). Don't call it stress drop, *Seismol. Res. Lett.* **68,** no. 1, 3–4.

Atkinson, G. M., and D. M. Boore (1995). Ground-motion relations for eastern North America, *Bull. Seismol. Soc. Am.* **85,** no. 1, 17–30.

Atkinson, G. M., and D. M. Boore (2006). Earthquake ground-motion prediction equations for eastern North America, *Bull. Seismol. Soc. Am.* **96,** no. 6, 2181–2205.

Atkinson, G. M., and D. M. Boore (2011). Modifications to existing ground-motion prediction equations in light of new data, *Bull. Seismol. Soc. Am.* **101,** no. 3, 1121–1135.

Atkinson, G. M., and R. F. Mereu (1992). The shape of ground motion attenuation curves in southeastern Canada, *Bull. Seismol. Soc. Am.* **82,** no. 5, 2014–2031.

Bay, F., D. Fäh, L. Malagnini, and D. Giardini (2003). Spectral shear-wave ground-motion scaling in Switzerland, *Bull. Seismol. Soc. Am.* **93,** no. 1, 414–429.

Bindi, D., M. Massa, L. Luzi, G. Ameri, F. Pacor, R. Puglia, and P. Augliera (2014). Pan-European ground-motion prediction equations for the average horizontal component of PGA, PGV, and 5%-damped PSA at spectral periods up to 3.0 s using the RESORCE dataset, *Bull. Earthq. Eng.* **12,** no. 1, 391–430.

Bommer, J. J., and A. Martínez-Pereira (1999). The effective duration of earthquake strong motion, *J. Earthq. Eng.* **3,** no. 2, 127–172.

Bommer, J. J., K. J. Coppersmith, R. T. Coppersmith, K. L. Hanson, A. Mangongolo, J. Neveling, E. M. Rathje, A. Rodriguez-Marek, F. Scherbaum, R. Shelembe, *et al.* (2014). A SSHAC level 3 probabilistic seismic hazard analysis for a new-build nuclear site in South Africa, *Earthq. Spectra* doi: 10.1193/060913EQS145M.

Boore, D. M. (1983). Stochastic simulation of high frequency ground motions based on seismological models of the radiated spectra, *Bull. Seismol. Soc. Am.* **73,** no. 6, 1865–1894.

Boore, D. M. (2003). Simulation of ground motion using the stochastic method, *Pure Appl. Geophys.* **160,** no. 3, 635–676.

Boore, D. M., and J. Boatwright (1984). Average body-wave radiation coefficients, *Bull. Seismol. Soc. Am.* **74,** no. 5, 1615–1621.

Boore, D. M., and J. J. Bommer (2005). Processing of strong-motion accelerograms: Needs, options and consequences, *Soil Dynam. Earthq. Eng.* **25,** no. 2, 93–115.

Boore, D. M., and C. A. Goulet (2014). The effect of sampling rate and anti-aliasing filters on high-frequency response spectra, *Bull. Earthq. Eng.* **12,** no. 1, 203–216.

Boore, D. M., and W. B. Joyner (1997). Site amplifications for generic rock sites, *Bull. Seismol. Soc. Am.* **87,** no. 2, 327–341.

Boore, D. M., and E. M. Thompson (2012). Empirical improvements for estimating earthquake response spectra with random-vibration theory, *Bull. Seismol. Soc. Am.* **102,** no. 2, 761–772.

Boore, D. M., and E. M. Thompson (2014). Path durations for use in the stochastic-method simulation of ground motions, *Bull. Seismol. Soc. Am.* **104,** no. 5, 2541–2552.

Boore, D. M., K. W. Campbell, and G. M. Atkinson (2010). Determination of stress parameters for eight well-recorded earthquakes in eastern North America, *Bull. Seismol. Soc. Am.* **100,** no. 4, 1632–1645.

Boore, D. M., J. P. Stewart, E. Seyhan, and G. M. Atkinson (2014). NGA-West 2 equations for predicting PGA, PGV, and 5% damped PSA for shallow crustal earthquakes, *Earthq. Spectra* **30,** no. 3, 1057–1085.

Bora, S. S., F. Scherbaum, N. Kuehn, and P. Stafford (2014). Fourier spectral- and duration models for the generation of response spectra adjustable to different source-, propagation-, and site conditions, *Bull. Earthq. Eng.* **12,** no. 1, 467–493.

Bozorgnia, Y., N. Abrahamson, A. Linda, D. A. Timothy, G. M. Atkinson, W. B. Baker, B. Annemarie, D. M. Boore, K. W. Campbell, B. Chiou, *et al.* (2014). NGA-West 2 research project, *Earthq. Spectra* **30,** no. 3, 973–987.

Brune, J. (1970). Tectonic stress and the spectra of seismic shear waves from earthquakes, *J. Geophys. Res.* **75,** no. 26, 4997–5009.

Brune, J. (1971). Correction, *J. Geophys. Res.* **76,** no. 20, 5002.

Campillo, M., M. Bouchon, and B. Massinon (1984). Theoretical study of the excitation, spectral characteristics, and geometrical attenuation of regional seismic phases, *Bull. Seismol. Soc. Am.* **74,** no. 1, 79–90.

Cartwright, D. E., and M. S. Longuet-Higgins (1956). The statistical distribution of the maxima of a random function, *Proc. Math. Phys. Sci.* **237,** no. 1209, 212–232.

Douglas, J., S. Akkar, G. Ameri, P.-Y. Bard, D. Bindi, J. J. Bommer, S. S. Bora, F. Cotton, B. Derras, M. Hermkes, *et al.* (2013). Comparisons among the five ground-motion models developed using RESORCE for the prediction of response spectral accelerations due to earthquakes in Europe and the Middle East, *Bull. Earthq. Eng.* **12,** no. 1, 341–358.

Douglas, J., B. Edwards, V. Convertito, N. Sharma, A. Tramelli, D. Kraaijpoel, B. M. Cabrera, N. Maercklin, and C. Troise (2014). Predicting ground motion from induced earthquakes in geothermal areas, *Bull. Seismol. Soc. Am.* **103,** no. 3, 1875–1897.

Drouet, S., S. Chevrot, F. Cotton, and A. Souriau (2008). Simultaneous inversion of source spectra, attenuation parameters, and site responses: Application to the data of the French Accelerometric Network, *Bull. Seismol. Soc. Am.* **98,** no. 1, 198–219.

Drouet, S., F. Cotton, and P. Guéguen (2010). V_{S30}, κ, regional attenuation and M_w from accelerograms: Application to magnitude 3–5 French earthquakes, *Geophys. J. Int.* **182,** no. 2, 880–898.

Edwards, B., and D. Fäh (2013a). Measurements of stress parameter and site attenuation from recordings of moderate to large earthquakes in Europe and the Middle East, *Geophys. J. Int.* **194,** no. 2, 1190–1202.

Edwards, B., and D. Fäh (2013b). A stochastic ground-motion model for Switzerland, *Bull. Seismol. Soc. Am.* **103,** no. 1, 78–98.

Edwards, B., D. Fäh, and D. Giardini (2011). Attenuation of seismic shear wave energy in Switzerland, *Geophys. J. Int.* **185,** no. 2, 967–984.

Edwards, B., C. Michel, V. Poggi, and D. Fäh (2013). Determination of site amplification from regional seismicity: Application to the Swiss National Seismic Networks, *Seismol. Res. Lett.* **84,** no. 4, 611–621.

Edwards, B., A. Rietbrock, J. J. Bommer, and B. Baptie (2008). The acquisition of source, path, and site effects from microearthquake recordings using Q tomography: Application to the United Kingdom, *Bull. Seismol. Soc. Am.* **98,** no. 4, 1915–1935.

Eshelby, J. D. (1957). The determination of the elastic field of an ellipsoidal inclusion, and related problems, *Proc. Math. Phys. Sci.* **241,** 376–396.

Gregor, N., N. A. Abrahamson, G. M. Atkinson, D. M. Boore, Y. Bozorgnia, K. W. Campbell, B. Chiou, I. M. Idriss, R. Kamai, E. Seyhan, *et al.* (2014). Comparison of NGA-West 2 GMPEs, *Earthq. Spectra* **30,** no. 3, 1179–1197.

Hanks, T. C., and H. Kanamori (1979). A moment magnitude scale, *J. Geophys. Res.* **84,** 2348–2350.

Hanks, T. C., and R. K. McGuire (1981). The character of high-frequency strong ground motion, *Bull. Seismol. Soc. Am.* **71,** no. 6, 2071–2095.

Joyner, W. B., R. E. Warrick, and T. E. Fumal (1981). The effect of quaternary alluvium on strong ground motion in the Coyote Lake, California, earthquake of 1979, *Bull. Seismol. Soc. Am.* **71,** no. 4, 1333–1349.

Ktenidou, O., F. Cotton, N. A. Abrahamson, and J. G. Anderson (2014). Taxonomy of κ: A review of definitions and estimation approaches targeted to applications, *Seismol. Res. Lett.* **85,** no. 1, 135–146.

Lermo, J., and F. J. Chávez-García (1993). Site effect evaluation using spectral ratios with only one station, *Bull. Seismol. Soc. Am.* **83,** no. 5, 1574–1594.

Madariaga, R. (1976). Dynamics of an expanding circular fault, *Bull. Seismol. Soc. Am.* **66,** no. 3, 639–666.

Mahani, A. B., and G. M. Atkinson (2012). Evaluation of functional forms for the attenuation of small-to-moderate earthquake response spectral amplitudes in North America, *Bull. Seismol. Soc. Am.* **102,** no. 6, 2714–2726.

Malagnini, L., R. B. Herrmann, and K. Koch (2000). Regional ground-motion scaling in central Europe, *Bull. Seismol. Soc. Am.* **90,** no. 4, 1052–1061.

Michel, C., B. Edwards, V. Poggi, J. Burjanek, D. Roten, C. Cauzzi, and D. Faeh (2014). Assessment of site effects in Alpine regions through systematic site characterization of seismic stations, *Bull. Seismol. Soc. Am.* **104,** no. 6, 2809–2826.

Morozov, I. B., C. Zhang, J. N. Duenow, E. A. Morozova, and S. B. Smithson (2008). Frequency dependence of coda Q, Part I: Numerical modeling and examples from peaceful nuclear explosions, *Bull. Seismol. Soc. Am.* **98,** no. 6, 2615–2628.

Okada, Y., K. Kasahara, S. Hori, K. Obara, S. Sekiguchi, H. Fujiwara, and A. Yamamoto (2004). Recent progress of seismic observation networks in Japan-Hi-net, F-net, K-NET and KiK-net, *Earth Planets Space* **56,** xv–xxviii.

Ou, G.-B., and R. B. Herrmann (1990). A statistical model for ground motion produced by earthquakes at local and regional distances, *Bull. Seismol. Soc. Am.* **80,** no. 6A, 1397–1417.

Raghu Kanth, S. T. G., and R. N. Iyengar (2007). Estimation of seismic spectral acceleration in peninsular India, *J. Earth Syst. Sci.* **116,** no. 3, 199–214.

Rietbrock, A., F. Strasser, and B. Edwards (2013). A stochastic earthquake ground-motion prediction model for the United Kingdom, *Bull. Seismol. Soc. Am.* **103,** no. 1, 57–77.

Rodriguez-Marek, A., E. M. Rathje, J. J. Bommer, F. Scherbaum, and P. J. Stafford (2014). Application of single-station sigma and site-response characterization in a probabilistic seismic-hazard analysis for a new nuclear site, *Bull. Seismol. Soc. Am.* **104,** no. 4, doi: 10.1785/0120130196.

Scherbaum, F. (1990). Combined inversion for the three-dimensional Q structure and source parameters using microearthquake spectra, *J. Geophys. Res.* **95,** no. B8, 12,423–12,438.

Thatcher, W., and T. C. Hanks (1973). Source parameters of southern California earthquakes, *J. Geophys. Res.* **78,** no. 35, 8547–8576.

Van Houtte, C., S. Drouet, and F. Cotton (2011). Analysis of the origins of κ (kappa) to compute hard rock to rock adjustment factors for GMPEs, *Bull. Seismol. Soc. Am.* **101,** no. 6, 2926–2941.

Vanmarcke, E. H., and S.-S. P. Lai (1980). Strong-motion duration and rms amplitude of earthquake records, *Bull. Seismol. Soc. Am.* **70,** no. 4, 1293–1307.

Yenier, E., and G. M. Atkinson (2014). Equivalent point-source modeling of moderate-to-large magnitude earthquakes and associated ground-motion saturation effects, *Bull. Seismol. Soc. Am.* **104,** no. 3, 1458–1478, doi: 10.1785/0120130147.

Institute of Earth and Environmental Science
University of Potsdam
Karl-Liebknecht-Street 24-25
14476 Potsdam, Germany
sanjay.singh@geo.uni-potsdam.de
fs@geo.uni-potsdam.de
(S.S.B., F.S.)

Pacific Earthquake Engineering Research Center
325 Davis Hall
University of California
Berkeley, California 94720-1792
kuehn@berkeley.edu
(N.K.)

Department of Civil and Environmental Engineering
Imperial College London
South Kensington Campus
London SW7 2AZ, United Kingdom
p.stafford@imperial.ac.uk
(P.S.)

Department of Earth, Ocean and Ecological Sciences
University of Liverpool
Liverpool L69 3GP, United Kingdom
Ben.Edwards@liverpool.ac.uk
(B.E.)

Manuscript received 3 October 2014;
Published Online 21 July 2015